J. Fluid Mech. (2022), *vol*. 947, A8, doi:10.1017/jfm.2022.624

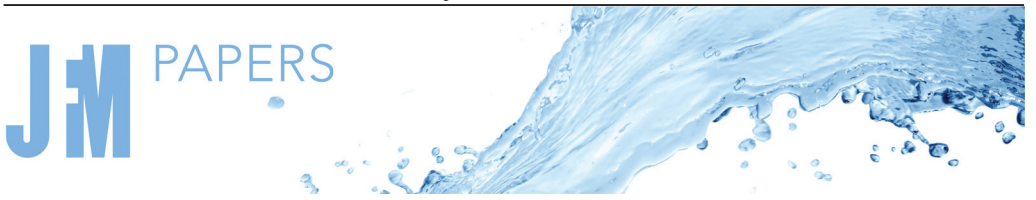

Hydrodynamic performance of slender swimmer: effect of travelling wavelength*

Li-Ming Chao[1], **Md. Mahbub Alam**[1],† **and Liang Cheng**[2,3]

[1]Center for Turbulence Control, Harbin Institute of Technology (Shenzhen), Shenzhen 518055, PR China

[2]Faculty of Infrastructure Engineering, Dalian University of Technology, Dalian, Liaoning, 116024, PR China

[3]School of Civil Engineering, University of Western Australia, Perth, WA 6009, Australia

(Received 15 October 2021; revised 24 June 2022; accepted 18 July 2022)

The impact of Strouhal number St (= 0.1–1.0), Reynolds number Re (= 50–2000) and dimensionless wavelength λ (= 0.5–2.0) on the hydrodynamic performance of a travelling wavy foil of a constant length is extensively investigated. The relationship of time-mean thrust with St, Re and λ is presented, suggesting that the propulsive force increases with increasing St, Re and λ. As such, the drag–thrust boundary advances as these parameters increase. A shorter λ makes the thrust steadier while a longer λ enhances the maximum instantaneous thrust. The latter is beneficial for prey to escape from a predator. The fluid added mass caused by the foil oscillation increases with St and λ but declines with Re (<500). Seven types of wake structures produced by the foil are identified, discussed and connected to thrust generation, showing how St, Re and λ affect the fluid dynamics, wake transition, vortex strength, wake jet, velocity, added mass, added damping, power input, efficiency and pressure profiles. The outcome of this work renders a physical basis for understanding the swimming of aquatic animals.

Key words: swimming/flying, flow-structure interactions

1. Introduction

The *Myllokunmingia* was a lonely swimmer several hundred million years ago (Shu *et al.* 1999) while aquatic swimmers exist everywhere in the ocean now. During this long history of evolution, swimming animals have mastered an exquisite capacity to control their body and the flow around themselves to efficiently cruise in water (Fish & Lauder 2006). There is no doubt that human beings admire the swimming skills of aquatic animals and hope to have a similar capacity.

† Email address for correspondence: alam@hit.edu.cn, alamm28@yahoo.com

* The online version of this article has been updated since original publication. A notice detailing the change has also been published.

With the development of science and technology, researchers have conscientiously considered swimming performance to be scientific, as explained in the light of fluid dynamics (Lighthill 1969; Triantafyllou, Triantafyllou & Yue 2000; Dabiri 2009; Lauder 2009; 2015; Shelley & Zhang 2011; Wu 2011; Chao, Cao & Pan 2017; Smits 2019; Alam & Muhammad 2020). Generally, natural swimmers share two similar propulsive strategies, including body-caudal-fin (BCF) and media-paired-fin propulsion (Breder 1926). The slender swimmers (such as fishes and mammals) always employ the BCF strategy to swim long distances largely at a constant speed. Moreover, the biological observations have shown that the BCF thrust-generation mechanisms can be further classified as oscillatory and undulatory, depending on the types of motion of the thrust-generating structure (Webb 1984).

A pitching foil pivoted at its leading edge is generally used to study the hydrodynamic performance of oscillatory BCF propulsion. Undergoing pitching oscillation, the foil generates time-mean thrust quadratically or cubically with Strouhal number St (Floryan *et al.* 2017; Van Buren *et al.* 2017; Alam & Muhammad 2020), where St is based on the pitching frequency f, peak-to-peak amplitude $2A_L$ and swimming speed U, i.e. $St = 2fA_L/U$. On the other hand, the propulsive force of a pitching foil is linked to the wake patterns generated by the foil (Zhang 2017; Chao *et al.* 2021*b*). The Kármán vortex (KV) wake and reverse Kármán vortex (RKV) wake are generally considered to produce drag and thrust, respectively (Von Kármán & Burgers 1934). Recently, several studies reported that the drag–thrust transition is not synchronous with the KV–RKV wake transition (e.g. Godoy-Diana, Aider & Wesfreid 2008). Floryan, Van Buren & Smits (2020) have reinterpreted results in the literature and pointed out that the wake-structure-based performance assessment of swimmers may be misleading. For example, Godoy-Diana *et al.* (2008) experimentally investigated the relationship between thrust force and wake structures of a pitching foil undergoing sinusoidal oscillations. They found that the KV–RKV wake transition precedes the drag–thrust transition. The asynchronization between the two transitions implies that the RKV wake may not necessarily produce thrust but may also lead to a drag. Following the work of Godoy-Diana *et al.* (2008), other works also validated the asynchronization between the drag–thrust transition and the KV–RKV wake transition of a pitching foil (Godoy-Diana *et al.* 2009; Marais *et al.* 2012; Deng, Sun & Shao 2015; Deng *et al.* 2016; Andersen *et al.* 2017; Chao *et al.* 2019; Chao, Alam & Ji 2021*a*; Chao *et al.* 2021*b*). Alam & Muhammad (2020) analysed the fluid dynamics based on inertia, using relative angular acceleration with respect to the foil, showing that the fluid dynamics is strongly dictated by the inertia of the foil. They mathematically developed a flow model based on Euler, Coriolis and centrifugal accelerations in a non-inertial frame to assimilate the physical insight into the thrust generation and power input. While Euler and Coriolis accelerations were involved in the power input, the centrifugal acceleration was linked to the thrust generation. The KV and RKV wakes were found to be the attributes of the drag and thrust, respectively, but not the origin of the thrust.

The undulatory BCF strategy is backbone undulation, which is a combination of two waves. One is a cyclic change of the curved body producing a lateral wave propagation in the caudal direction, and the other is every single point on the body undergoing a sinusoidal track in a horizontal plane as the consequence of the wave propagation (Gray 1933). Therefore, the movement of the slender swimmer can be appropriately considered as the fish-like foil undergoing a streamwise travelling wavy motion that is used by *anguilliform*, *carangiform* and *subcarangiform* swimmers (Carling, Williams & Bowtell 1998; Liao *et al.* 2003; Kern & Koumoutsakos 2006). Similar to a pitching foil, the travelling wavy foil also showed that the foil kinematics would directly affect the

hydrodynamic performance of the foil (Barrett *et al.* 1999; Shen *et al.* 2003; Dong & Lu 2005; Lu & Yin 2005; Deng, Shao & Ren 2006; Zhang *et al.* 2018). Lu & Yin (2005) have investigated the propulsive performance of a fish-like travelling wavy wall and found that the undulation amplitude and the oscillation frequency of the travelling wavy motion are two important parameters in determining the thrust generation. The propulsive force produced by the travelling wavy foil increases with increasing foil undulation amplitude.

Compared with the pitching foil, the travelling wavy foil complies better with the swimming behaviour of the slender swimmer (Smits 2019). Although researchers have made a considerable effort to understand the hydrodynamic performance of a fish-like foil undergoing travelling wavy motion, the effect of the foil deforming characteristics is not well understood. The different slender swimmers essentially employ different strategies to bend their bodies (Breder 1926). A single specific swimmer even has different deforming techniques under different conditions, such as the fish that uses C-start (C-shaped) deformation during the survival behaviour (Gazzola, Van Rees & Koumoutsakos 2012). However, to the authors' knowledge, no systematic investigation has been done on how the deforming characteristics affect the propulsive performance of a travelling wavy foil. On the other hand, we also noted that the previous works on the travelling wavy foil always kept a constant projected length of the foil body in the streamwise direction. This is, however, not the case in reality as the projected length will be smaller when the wave amplitude is larger. In this work, we therefore attempt to systematically investigate the hydrodynamic performance of a travelling wavy foil with varying foil kinematics (Strouhal number), fluid properties (Reynolds number) and foil deforming characteristics (wavelength), with the foil length kept constant to replicate the native slender swimmer. Moreover, the results for the travelling wavy foil configuration are compared with those for the pitching foil configuration.

2. Method

2.1. *Problem formulations*

A schematic of the flow configuration is presented in figure 1(*a*). A two-dimensional NACA0012 foil with chord-length of L is placed in a uniform flow of velocity U in the x-direction, where the leading edge of the foil is located at the origin of the Cartesian coordinate system. The movement of the foil midline can be expressed by the following travelling wavy equation:

$$\left.\begin{array}{c} y(x,t) = A(x)\sin\left[2\pi\left(\dfrac{x}{\lambda_r} - \dfrac{t}{T}\right)\right] \\ \displaystyle\int_0^{L_s(t)} \sqrt{\{1+(\partial y/\partial x)^2\}}\,\mathrm{d}x = L \end{array}\right\}, \tag{2.1}$$

where $A(x)$ is the swimming amplitude function, usually considered as a polynomial $A(x) = a_0 + a_1 x + a_2 x^2$ (Videler 1993), x is measured from the leading edge of the foil, y is the lateral displacement of the foil midline, λ_r is the real wavelength defined in figure 1(*b*), t is the instantaneous time, T is the undulation period and $L_s(t)$ denotes projected length of the foil on the x-axis (streamwise direction), giving $L_s(t) \leq L$. Without a loss of generality, $a_0 = a_2 = 0$ and $a_1 = 0.05$ are employed to determine the foil undulation. In addition, the dimensionless wavelength λ normalized by L (i.e. $\lambda = \lambda_r/L$) is employed to describe the foil deformation. With $x \leq L$, only the first formula in (2.1) was employed to describe the fish-like locomotion in the literature (Lu & Yin 2005; Deng *et al.* 2006;

Xiao *et al.* 2011; Gupta *et al.* 2021), where the length of the foil midline varies with time and $L_s(t)$ is kept constant. This is, however, not the case in reality; the fish-like swimmer cannot change its midline body length. To follow the kinematics of a real swimmer, both the foil midline length and the included area are kept constant, with the foil midline computed from (2.1). The foil surface is given by maintaining the normal distance (e.g. h_s at an arbitrary point on the midline) from the midline constant for the deformed and undeformed foils. For example, consider that h_s is the distance between point A on the foil midline and point B (normal to the midline) on the foil surface when the foil is straight, undeformed (figure 1*c*). At each time step, the line AB normal to the deformed midline can be computed from the differential form of (2.1). The new location of point B on the foil surface is then pinpointed with $AB = h_s$. A typical envelope of the undulation is illustrated in figure 1(*d*), where it is easy to understand that $L_s(t)$ is a time-dependent variable, with $L_s(t) = L$ corresponding to the straight midline (dashed blue line), not undulating.

The $L_s(t) < L$ always holds during the travelling wavy motion; as an example, the waves for $\lambda = 0.50$ are shown in figure 2(*a*) at different instants. Naturally, the time-mean midline length $\overline{L_s} = (1/T)\int_t^{t+T} L_s(t)\,\mathrm{d}t$ is also smaller than L. The effect of the foil deformation on the foil modality is described in figure 2(*b*), where $\overline{L_s}/L$ increases with increasing λ. Figure 2(*b*) also displays the maximum and minimum L_s (i.e. L_{s-max} and L_{s-min}) to see how L_s changes with time. It is seen that a smaller λ results in a greater fluctuation in $L_s(t)$, which can be viewed from the gap between the L_{s-max} and L_{s-min} (figure 2*b*). With an example at $\lambda = 1.0$ in figure 2(*b*) (inset), the $L_s(t)$ is minimum at the ends of the up and down strokes of the foil tail while maximum when the amplitude equals a half of the maximum swimming amplitude. The $L_s(t)$ at zero amplitude is slightly larger than L_{s-min}.

The Strouhal number and Reynolds number are defined as

$$St = 2A_L/UT, \tag{2.2}$$

and

$$Re = UL/\nu, \tag{2.3}$$

where A_L ($= 0.05L$) is the tail amplitude and ν is the kinematic viscosity of the fluid. The time-mean thrust coefficient $\bar{C}_T$ in one oscillation period is defined as

$$\bar{C}_T = \frac{1}{T}\int_t^{t+T} C_T\,\mathrm{d}t = \frac{1}{T}\int_t^{t+T} -\frac{F_x(t)}{0.5\rho U^2 L}\,\mathrm{d}t, \tag{2.4}$$

where C_T is the instantaneous thrust coefficient, $F_x(t)$ is the drag (x-direction) force acting on the foil and ρ is the density of the fluid. Therefore, $\bar{C}_T > 0$ and $\bar{C}_T < 0$ represent the foil generating time-mean thrust and experiencing time-mean drag, respectively, while $\bar{C}_T = 0$ is the drag–thrust transition boundary.

2.2. *Numerical approach*

All numerical experiments are conducted at $Re \leq 2000$ giving a laminar flow (Gazzola, Argentina & Mahadevan 2014). The unsteady flow field around the foil is simulated using the commercially available computational fluid dynamics (CFD) package Fluent 14.0. For a Newtonian fluid, the governing equations describing unsteady incompressible flow are

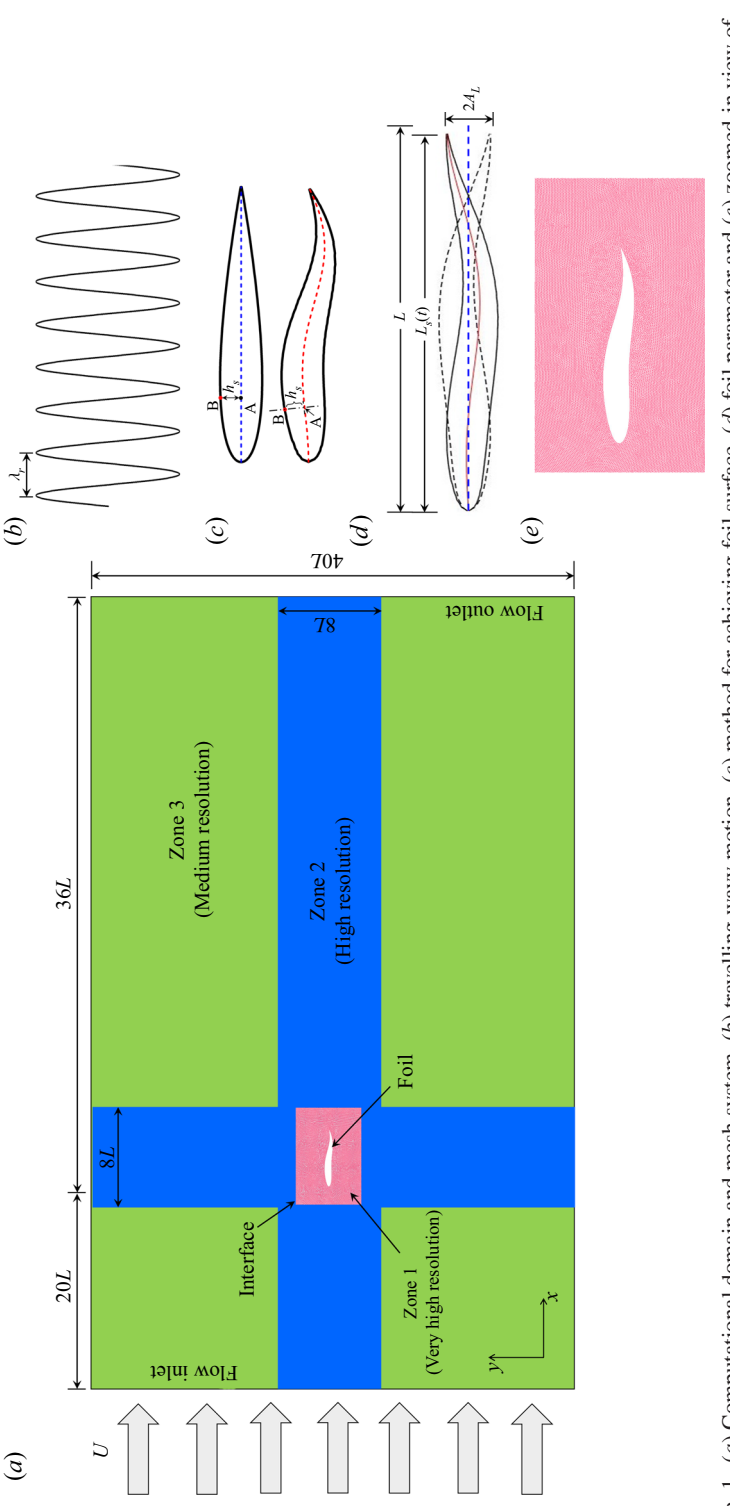

Figure 1. (*a*) Computational domain and mesh system, (*b*) travelling wavy motion, (*c*) method for achieving foil surface, (*d*) foil parameter and (*e*) zoomed-in view of mesh around the foil.

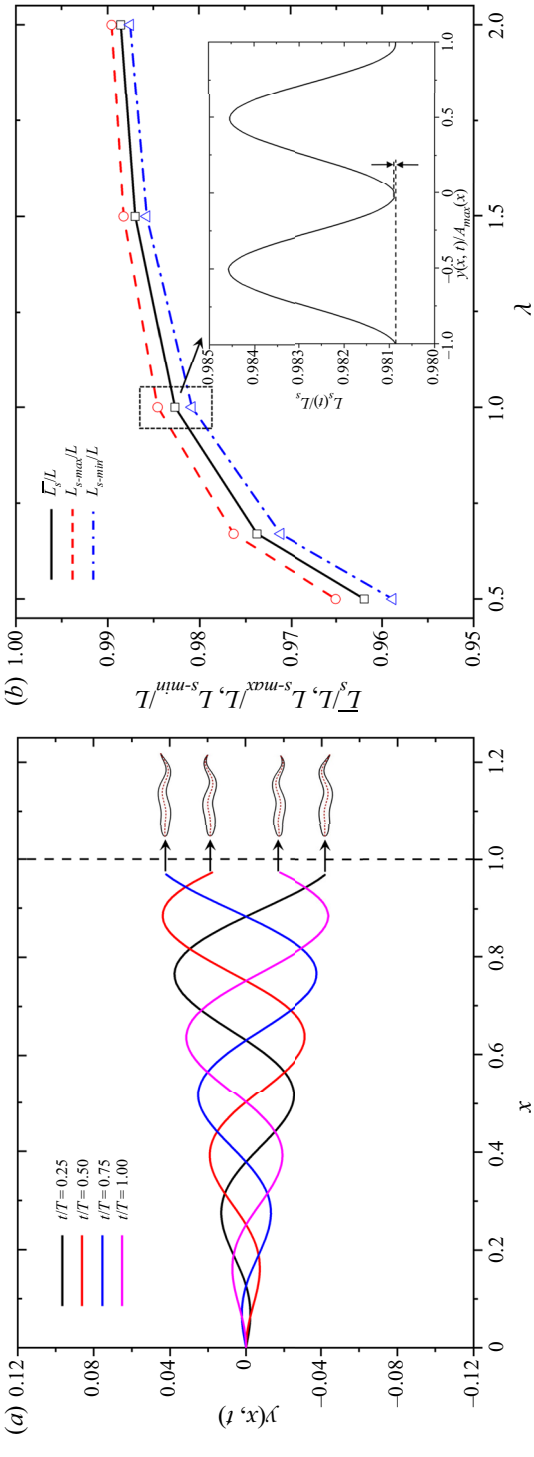

Figure 2. (*a*) Travelling wavy motion of foil at different instants with $\lambda = 0.50$. (*b*) Dependence of $\overline{L_s}/L$, L_{s-max}/L and L_{s-min}/L on λ where L_{s-max} and L_{s-min} are the maximum and minimum $L_s(t)$ in one oscillation period, respectively. Here, $A_{max}(x)$ is the maximum amplitude.

the mass and momentum conservation equations

$$\nabla \cdot \boldsymbol{u} = 0, \tag{2.5}$$

and

$$\frac{\mathrm{D}\boldsymbol{u}}{\mathrm{D}t} = -\frac{1}{\rho}\nabla p + \nu\nabla^2\boldsymbol{u}, \tag{2.6}$$

where $\boldsymbol{u}$ denotes the velocity vector and p is the static pressure.

The finite-volume method is used to achieve the spatial discretization of the Navier–Stokes equations (2.5) and (2.6). The temporal discretization is done using the second-order backward-implicit scheme. The semi-implicit method for pressure linked equations (SIMPLE) algorithm is used to achieve the pressure–velocity coupling of the continuity equation (2.5). Moreover, the Gauss–Seidel linear equation solver is employed to solve the discretized equations.

The computational domain is rectangular with a size of $56L \times 40L$ (figure 1*a*). The inlet velocity boundary is at a distance of $20L$ from the leading edge of the foil, with $\boldsymbol{u} = (U,$ 0) and $\partial p/\partial x = 0$ while the outflow boundary is $36L$ downstream, with $u/x = (0,\ 0)$ and $\partial p/\partial x = 0$ (no-stress outflow boundary conditions). The slip wall condition is used for the upper and lower boundaries located symmetrically $40L$ apart (Bos *et al.* 2008).

The flow domain consists of three grid zones: 1, 2 and 3 (figure 1*a*). Zone 1 is regular and has a very high resolution in unstructured grids around the foil while zone 2 is of high resolution, where a large velocity gradient is expected. The region away from the wake is zone 3 that has a medium resolution. In both zones 2 and 3, structured meshes are used. The first cell is placed at a distance of $10^{-3}L$ from the foil surface (figure 1*e*). The locomotion of foil in the computational domain is achieved using a dynamic grid scheme implemented in FLUENT. At each updated time instant, the foil motion is determined using (2.1) while the cells around the foil are regenerated and smoothed using the FLUENT DEFINE_GRID_MOTION function in regridding and smoothing processes.

Mesh and time-step independence tests were also performed at $(St, Re, \lambda) = (0.5, 1000,$ 1.0). At the time step of $\Delta t = 4 \times 10^{-4}T$ (obtained using (11) in Kinsey & Dumas 2008), the grid-independence test is done for grid numbers 9.8×10^5 (M1), 2.24×10^6 (M2) and 9.5×10^6 (M3) corresponding to 191, 401 and 891 points on the surface of the foil, respectively. The time histories of the thrust coefficient over two cycles are shown in figure 3(*a*) for the three grid systems. It indicates no significant difference in thrust between M2 and M3. We, therefore, adopted M2 for the computations. With M2, three time steps of $1.0 \times 10^{-3}T$ ($\Delta t1$), $4.0 \times 10^{-4}T$ ($\Delta t2$), $2.0 \times 10^{-5}T$ ($\Delta t3$) are tested. The computed results shown in figure 3(*b*) suggest that $\Delta t2$ is enough to ensure accuracy and save computational resources. The time step with mesh M2 is further validated for $St = 1.0$ corresponding to the smallest period examined. Table 1 shows the time-step-independence results when the time step is reduced from $\Delta t1 = 1.0 \times 10^{-3}T$ to $\Delta t3 = 2.0 \times 10^{-5}T$. Given that the difference in $\bar{C}_T$ between $\Delta t2 = 4.0 \times 10^{-4}T$ and $\Delta t3 = 2.0 \times 10^{-5}T$ is 0.037 % only, $\Delta t2$ ($= 4.0 \times 10^{-4}T$) is assumed small enough to ensure accuracy.

Before conducting extensive simulations, we simulated thrust generation of a travelling wavy foil to compare our results with the results of Xiao *et al.* (2011) at $Re = 45\ 000$. They investigated the near wake interaction between a travelling wavy foil and a D-section cylinder, using the same numerical technique and foil geometry as ours. Xiao *et al.*'s results are thus considered the benchmark to validate our work although their Reynolds number is larger than ours. A comparison of C_T between the present and Xiao *et al.*'s works at $(St, Re, \lambda) = (0.23, 45\ 000, 1.15)$ is made in figure 3(*c*) while the differences

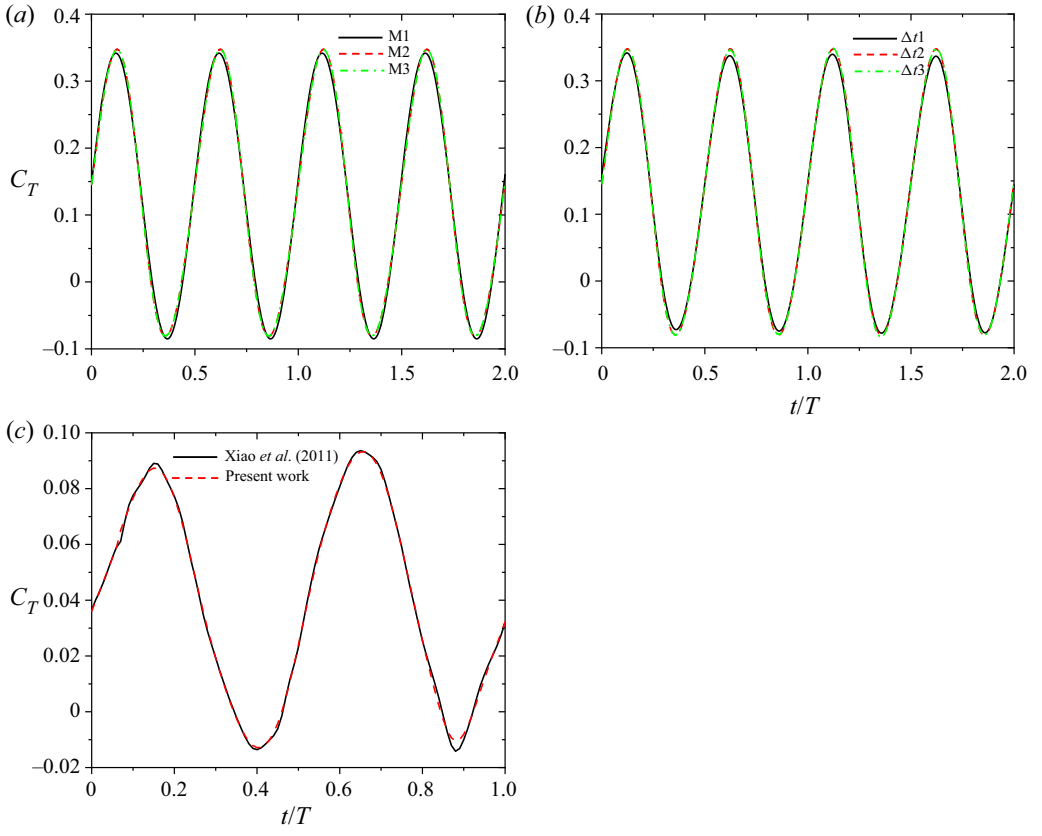

Figure 3. Numerical validations. (*a*,*b*) Mesh and time-step-independence test at (St, Re, λ) = (0.5, 1000, 1.0). (*c*) Comparison between the results of present numerical method and those of Xiao *et al.* (2011) at (St, Re, λ) = (0.23, 45000, 1.15).

	$\bar{C}_T$	Difference in $\bar{C}_T$ (%)
$\Delta t1\ (=1.0\times10^{-3}T)$	1.2892	4.685
$\Delta t2\ (=4.0\times10^{-4}T)$	1.3501	0.037
$\Delta t3\ (=2.0\times10^{-5}T)$	1.3496	—

Table 1. Time-step-independence test at (St, Re, λ) = (1.0, 1000, 1.0).

in the maximum thrust coefficient $C_{T_{max}}$ and $\bar{C}_T$ between the Xiao *et al.*'s (2011) and present works are listed in table 2. A good agreement in C_T is achieved between the present and Xiao *et al.*'s study, the differences in $C_{T_{max}}$ and $\bar{C}_T$ being 0.438 % and 0.036 %, respectively. More discussion on the laminar flow model will be presented in Appendix A.2.

3. Results and Discussions

To investigate the thrust generation and wake structures of the travelling wavy foil, we systematically studied the time-mean thrust force acting on the foil for $St = 0.1$–1.0 with $\Delta St = 0.1$, for $Re = 50$, 100, 250, 500, 750, 1000, 1250, 1500, 1750 and 2000, and for $\lambda = 0.50$, 0.67, 1.0, 1.5 and 2.0. The results for the thrust generation are presented

	$C_{T_{max}}$	$\bar{C}_T$
Xiao *et al.* (2011)	0.09361	0.040217
Present	0.0932	0.040203
Difference (%)	0.438	0.036

Table 2. Comparisons of $C_{T_{max}}$ and $\bar{C}_T$ between Xiao *et al.*'s (2011) and present works.

first, followed by the results for the added mass, added damping, power, efficiency and wake structures. In particular, the dependence of thrust on λ is investigated up to $\lambda = \infty$. In the present study, all cases were simulated for 40 undulation periods to ensure statistically steady thrust signals and wake structures, while the averages were made over the last 10 simulation periods (from 31th to 40th periods), given that the simulations were statistically converged after the 5–15th period, depending on *Re*, λ and *St*.

3.1. *Dependence of thrust on Re, St and* λ

Figure 4(*a*)–4(*e*) illustrates the dependence of $\bar{C}_T$ on *Re*, *St* and λ. The solid black line represents the drag–thrust boundary ($\bar{C}_T = 0$). For a given λ, the $\bar{C}_T$ increases from negative (lower-left corner) to positive (upper right corner) when *St* and *Re* are increased. The travelling wavy foil cannot produce thrust when *Re* and *St* are low but can when *Re* and *St* are sufficiently high, depending on λ. Interestingly, $\bar{C}_T$ is equally dependent on *St* and *Re* in the drag regime ($\bar{C}_T < 0$) but more sensitive to *St* in the thrust regime ($\bar{C}_T > 0$). This observation indicates that viscous (*Re*) and inertia (*St*) effects both play important roles in fluid dynamics in the drag regime while the inertia effect dictates the fluid dynamics in the thrust regime. For a given set of *St* and *Re*, an increase in λ leads to an enhancement in $\bar{C}_T$. As such, the drag–thrust boundary shifts to smaller *St* and *Re* when λ is increased. With the same *St* and λ, $\bar{C}_T$ gets higher at a higher *Re*, i.e. having acceleration is easier at a higher speed. The reason is that the viscous effect weakens and the added mass lessens (will be shown later) when *Re* is increased. On the other hand, a foil with a smaller λ hinders the streamwise flow over the surface, resulting in a smaller thrust generation. When the stationary wavy foil ($St = 0$) retains a travelling wavy shape (as sketched in figure 4*a–e*), it would experience a thrust ($\bar{C}_{T0}$) that is negative (i.e. drag). Apparently, $\bar{C}_{T0}$ would be dependent on *Re* as shown in figure 4(*f*), where $\bar{C}_{T0}$ declines with *Re* as $\bar{C}_{T0} = -6.13Re^{-0.6}$. Das, Shukla & Govardhan (2016) showed that a straight NACA0012 foil at zero attack angle incurs $\bar{C}_{T0} = -5.96Re^{-0.56}$ that is smaller in magnitude than the present counterpart. This is plausible as an undulated foil would experience a higher drag than a straight foil.

Based on the previous studies on the scaling of a flapping foil (Floryan *et al.* 2017; Van Buren *et al.* 2017; Alam & Muhammad 2020), the relationship of $\bar{C}_T$ with *St*, *Re* and λ can be written as

$$\bar{C}_T = c_0 Re^a St^b \lambda^c + \bar{C}_{T0}. \tag{3.1}$$

Thus, λ naturally describes how the flow is transported from the leading edge to the trailing. When $\lambda = 1$, the flow transportation time T_λ (i.e. wave travelling time from the leading edge to the trailing) equals the travelling wavy motion period T. On the other hand, the $T_\lambda > T$ and $T_\lambda < T$ emerge at $\lambda < 1$ and $\lambda > 1$, respectively. This suggests that their relationship is linear, giving the exponent c of λ in (3.1) as $c = 1$. Based on the

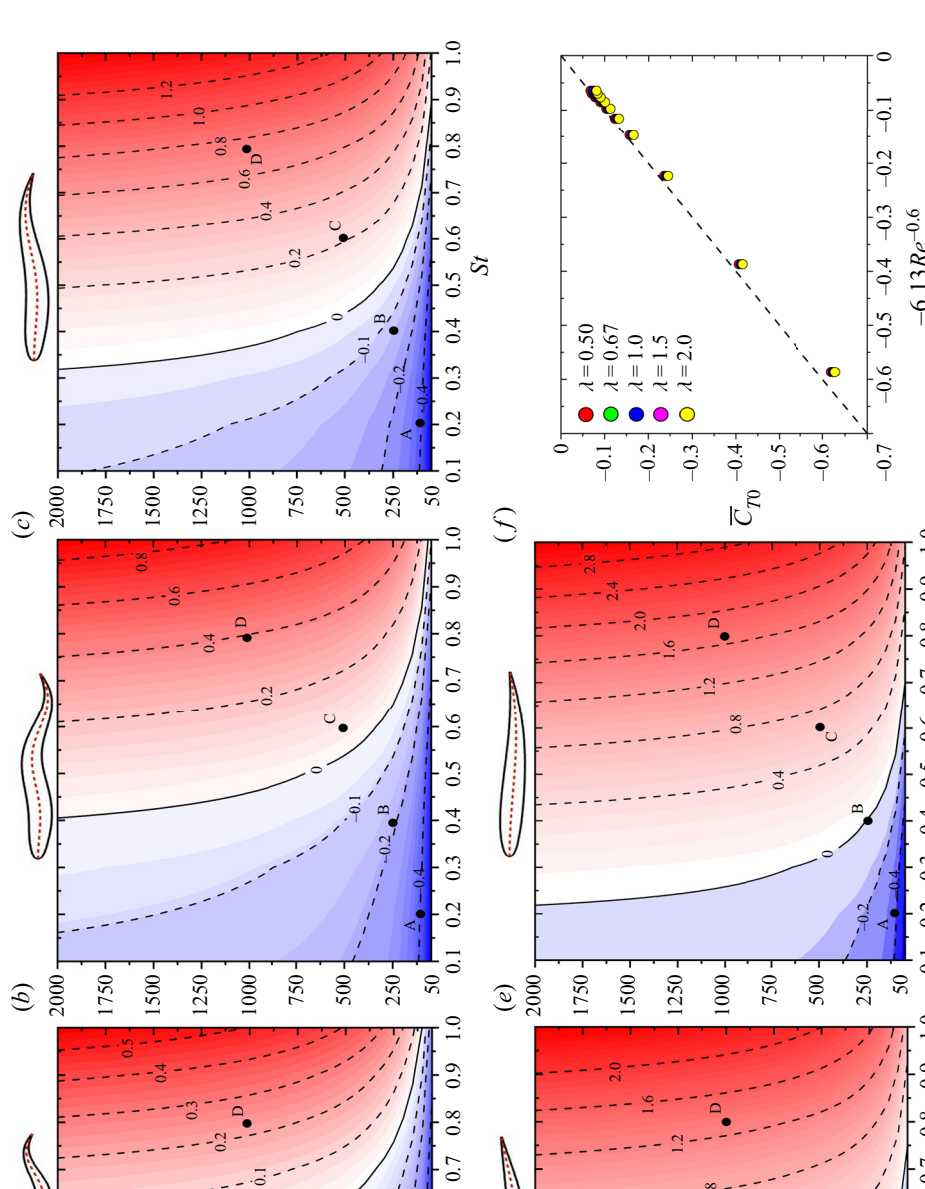

Figure 4. (*a–e*) Dependence of time-mean thrust on Re, St and λ for the travelling wavy foil. A, B, C and D are four points selected as A ($St = 0.2$, $Re = 100$) in the drag regime, B (0.4, 250) close to drag–thrust boundary at high λ, C (0.6, 500) close to drag–thrust boundary at small λ and D (0.8,1000) in thrust regime, to show the influence of λ on instantaneous thrust in figure 9. (*f*) Dependence of time-mean thrust force of a stationary foil on Re. (*a*) $\lambda = 0.50$, (*b*) $\lambda = 0.67$, (*c*) $\lambda = 1.0$, (*d*) $\lambda = 1.5$, (*e*) $\lambda = 2.0$.

theoretical model involving the Euler angular, Coriolis and centrifugal accelerations of a cone of fluid around the foil, Alam & Muhammad (2020) theoretically showed that the relationship between $\bar{C}_T$ and St can be considered as $\bar{C}_T \propto St^3$. Thus, (3.1) can be written as

$$\bar{C}_T = c_0 Re^a St^3 \lambda^1 + \bar{C}_{T0}. \tag{3.2}$$

The linear least-squares regression for a given Re is used to find the relationship between $\bar{C}_T$, St and λ, giving $\bar{C}_T = c_1 St^3 \lambda + c_2$, where four examples are illustrated in figure 5. The relationship provides $c_1 = 0.904$, 1.388, 1.533 and 1.704 and $c_2 = -0.3848$, -0.1543, -0.0951 and -0.061 for $Re = 100$, 500, 1000 and 2000, respectively (figure 5*a–d*). The dependence of c_1 and c_2 on Re (for all Re examined) can be observed from figure 6(*a*), where their dependencies are reprocessed as $c_1 = 0.36Re^{0.208}$ and $c_2 = -6.13Re^{-0.6}$ (the $\bar{C}_{T0}$ scaling). Therefore, the relationship of $\bar{C}_T$ with St, Re and λ can be unified as

$$\bar{C}_T = 0.36Re^{0.208} St^3 \lambda - 6.13Re^{-0.6}. \tag{3.3}$$

Here, $\bar{C}_{T0} = -6.13Re^{-0.6}$, with exponent -0.6 close to that of Re in $1/\sqrt{Re}$, indicates the dominance of fluid resistance forces from the unseparated boundary layer over the stationary foil surface. Equation (3.3) displays how St, Re and λ affect the propulsive force on the foil. It is easy to understand from (3.3) that the thrust generation ($\bar{C}_T > 0$) is largely dictated by St and λ, especially by St. The $\bar{C}_T$ grows slowly with increasing Re, which essentially reflects the viscous flow resistance weakening with increasing Re. In particular, when Re is large enough, the second term on the right-hand side approaches zero, which gives $\bar{C}_T = 0.36Re^{0.208} St^3 \lambda$. When the foil is stationary ($St = 0$), (3.3) degenerates into $\bar{C}_T = -6.13Re^{-0.6}$, i.e. the $\bar{C}_{T0}$ scaling. To see how much (3.3) is capable of collapsing all simulated data, $\bar{C}_T$ is presented against $0.36Re^{0.208} St^3 \lambda - 6.13Re^{-0.6}$ in figure 6(*b*). The data for different values of λ collapse well on the line, suggesting that (3.3) can be used to estimate $\bar{C}_T$ for any values of St, Re and λ. Alam & Muhammad (2020) proposed a model of flow around a pitching hydrofoil. The flow model explicitly reflected the produced torque and thrust, involving Euler angular, Coriolis and centrifugal accelerations of a cone of fluid around the foil. They found that torque (power input) is required to compensate Euler and Coriolis accelerations, and thrust (output) is essentially produced from the centrifugal acceleration. The developed theoretical model showed that thrust is proportional to St^3.

Since Re appears in both terms on the right-hand side of (3.3), the dependence of $\bar{C}_T$ on Re may not be straightforward. We therefore calculate $\partial \bar{C}_T/\partial Re$ ($= 0.07488Re^{-0.792} St^3 \lambda + 3.678Re^{-1.6}$) from (3.3) to investigate the effect of Re on $\bar{C}_T$. Figure 7(*a*) displays $\partial \bar{C}_T/\partial Re$ against Re at $St = 0.1$, 0.5 and 1.0 with $\lambda = 1.25$. The value of $\partial \bar{C}_T/\partial Re$ declines with increasing Re regardless of St while a smaller St leads to a smaller $\partial \bar{C}_T/\partial Re$. The observation suggests that manoeuvring is easier at a smaller Re and a higher St. The value of $\partial \bar{C}_T/\partial Re$ sharply drops at $Re \leq 250{-}600$ (depending on St) and reaches its asymptotically small value at $Re \geq 250{-}600$ (depending on St). That is, the effect of Re on $\bar{C}_T$ is predominant in the former Re range and insignificant in the latter Re range. To see how this information is dependent on λ and other St values, contours of $\partial \bar{C}_T/\partial Re$ are presented in the St–Re plane for different λ values examined (figure 7*b*). The value of $\partial \bar{C}_T/\partial Re$ degrades when λ is decreased, which can be observed from the higher $\partial \bar{C}_T/\partial Re$ region shrinking with decreasing λ. This again suggests that a higher λ is required for agility and manoeuvring. The $\partial \bar{C}_T/\partial Re$ contour can also be employed to understand the survival hydrodynamics of swimmers. A few interesting natural observations can be linked to the results in figure 7. Firstly, the prey is generally smaller in size than the concerned

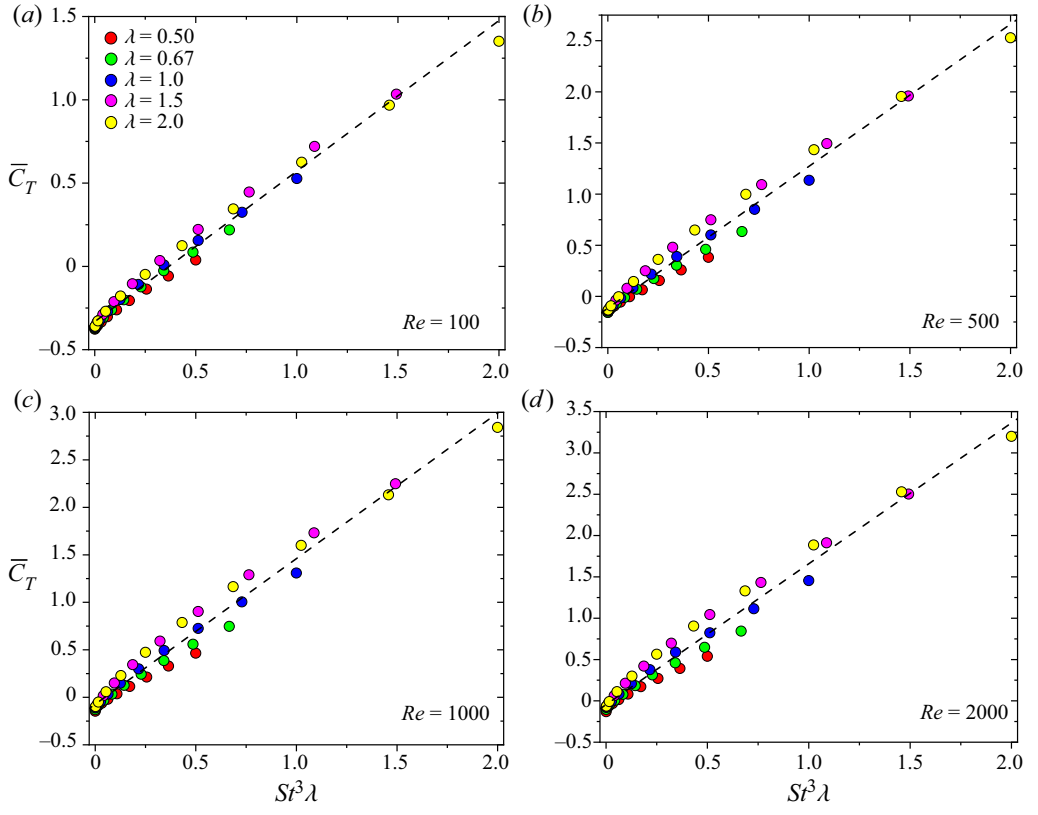

Figure 5. Time-mean thrust coefficient $\bar{C}_T$ as a function of Strouhal number St and wavelength λ, denoted as $\bar{C}_T = c_1 St^3\lambda + c_2$. The dashed line is the linear least-squares regression line.

predator, hence the former having a smaller Re. This facilitates the prey having a greater agility or acceleration to escape from the predator. Secondly, a larger St and λ are beneficial to generating larger acceleration, which is consistent with Triantafyllou, Weymouth & Miao's (2015) observation that a swimmer usually adopts a larger St and λ during the predator–prey behaviour. When Re is sufficiently high due to increased speed, the Re effect disappears and the predator–prey game relies on St and λ only. Equation (3.3) further reflects that $\partial\bar{C}_T/\partial St$ is proportional to $Re^{0.208}$ and λ, which suggests that the enhancement of $\bar{C}_T$ with St is larger at a higher Re and a larger λ. The scenario is also reflected in figure 4, with the contour lines having smaller slopes at smaller Re and *vice versa*. A predator usually large in size (hence higher Re) gets benefits of thrust enhancement with increasing St.

The drag–thrust boundary ($\bar{C}_T = 0$) is found to be dependent on λ. It is worth finding the relationship between St, Re and λ corresponding to the drag–thrust boundary (figure 4). The drag–thrust boundary can be obtained from (3.3) by plugging $\bar{C}_T = 0$, i.e.

$$St = 2.57 Re^{-0.27}\lambda^{-1/3}. \tag{3.4}$$

Equation (3.4) reflects that the drag–thrust boundary in the St-Re domain advances with increasing λ, as illustrated in figure 4. This result conforms with the previous work by Gazzola *et al.* (2014). At a given λ, the boundary follows $St \propto Re^{-0.27}$, which indicates that the drag–thrust boundary is more sensitive to St at smaller Re, and

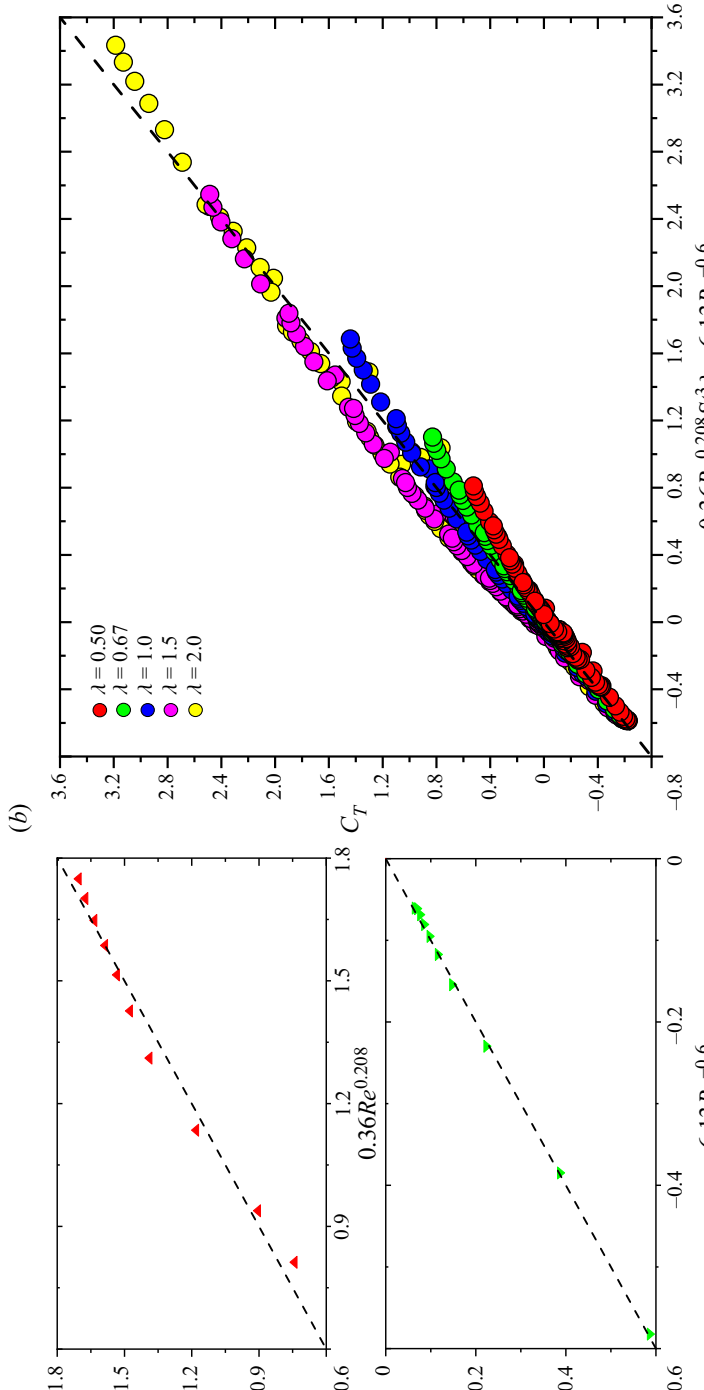

Figure 6. (*a*) Dependence of c_1 and c_2 on Re. (*b*) Relationship of $\bar{C}_T$ with St, Re and λ for the travelling wavy foil. The dashed lines denote the proportional function with coefficient equal to one.

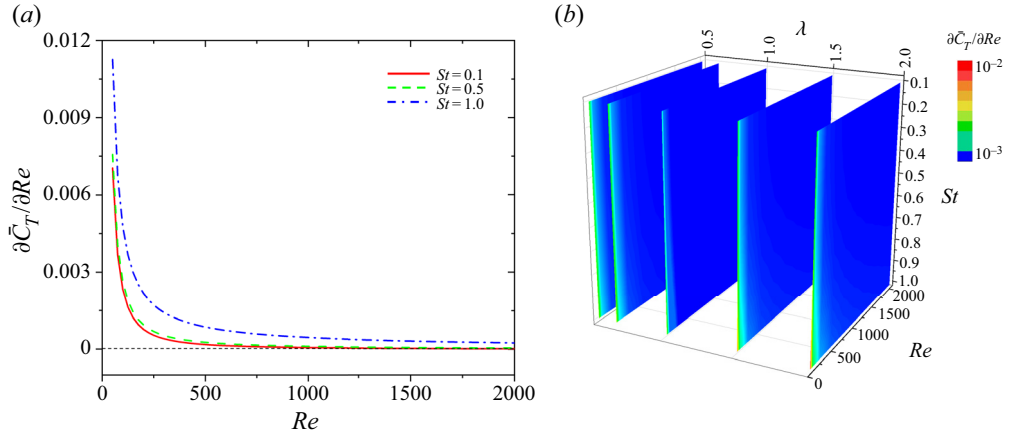

Figure 7. (*a*) Variation in $\partial\bar{C}_T/\partial Re$ with Re at $\lambda = 1.25$. (*b*) Relationship of $\partial\bar{C}_T/\partial Re$ with St, Re and λ.

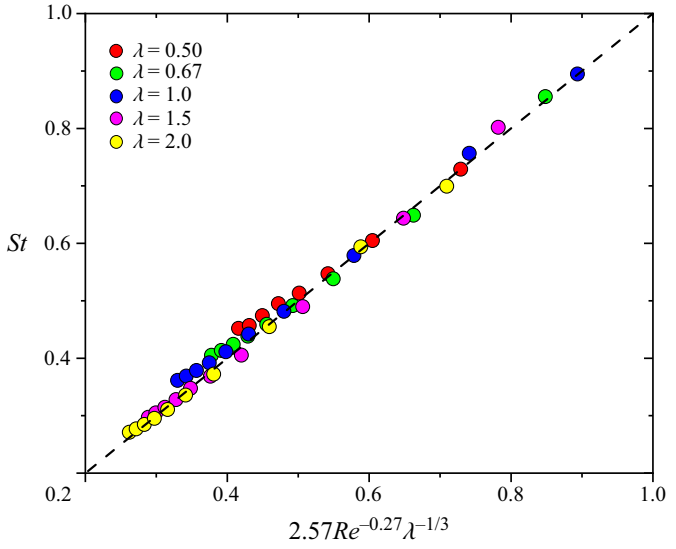

Figure 8. Dependence of drag–thrust boundary on Strouhal number, Reynolds number and wavelength for the travelling wavy foil. The drag–thrust boundary corresponds to $St = 2.57Re^{-0.27}\lambda^{-1/3}$ marked by the dashed line that fits well with the present data.

vice versa. The drag–thrust boundary can be considered as the native swimmer cruising at a constant speed, with no acceleration and no deceleration. Here, we again refer to the work of Gazzola *et al.* (2014) where the locomotion of a cursing swimmer conforms to $St \propto Re^{-0.25}$ when $Re \leq 2000$. The present results and relationship conform with the biological observations (Gazzola *et al.* 2014) while the effect of the deforming strategy (λ) on the cruising locomotion is first presented in this work (figure 8). When cruising in the water, different swimmers employ different deforming strategies, and hence different swimming strategies (e.g. St). It is the biological diversity of aquatic locomotion. Since λ values adopted by aquatic animals are restricted in a limited scope (Lucas *et al.* 2014), it is easy to understand that most cruising swimmers operate in a relatively narrow range of St, such as $0.2 \leq St \leq 0.4$ (Taylor, Nudds & Thomas 2003; Eloy 2012; Gazzola *et al.*

2014). In addition, the swimmer can generate accelerating or decelerating locomotion by increasing or decreasing λ, which provides a simple way to control the motion. For example, a swimmer can have a longer λ at the start of locomotion, a moderate λ to swim at a constant speed and a shorter λ to reduce the speed (deceleration).

It should be noted that travelling wavy motion can be considered as the pitching motion when $\lambda \to \infty$. We undertook numerical simulations for $\lambda = 2.5$, 3.0, 3.5, 4.0, 4.5, 5.0, 7.5, 10, 25, 50, 100, 1000, 10 000 and ∞ (straight foil, pitching) at $St = 0.5$ and $Re = 1000$ in order to understand how the results approach those for pitching motion of a straight foil. The foil kinematics gradually modifies from travelling wavy motion to pitching motion when λ is increased to ∞ (figure 9*a*). The foil with $\lambda = \infty$ corresponds to a pitching angle of 2.867°, given $a_1 = 0.05$. Interestingly, $\bar{C}_T$ escalates for $0.50 \leq \lambda \leq 7.5$ before declining for $7.5 < \lambda < 100$. The value of $\bar{C}_T$ at $\lambda = 100$–10 000 is the same as that at $\lambda = \infty$ (figure 9*b*). The zoom-in view of figure 9(*b*) (shown as an inset) demonstrates that the linearity of $\bar{C}_T$ with λ (i.e. $\bar{C}_T \propto \lambda$) prevails at $\lambda \leq 2.5$. To understand the thrust generation at $\lambda > 100$, simulations were conducted at $\lambda = 1000$ which provides the same $\bar{C}_T$ as $\lambda = \infty$ (figure 9*b*). Figure 9(*c*) shows $\bar{C}_T$ contours in the *St*–*Re* plane for $St = 0.1$–1.0 with $\Delta St = 0.1$ and $Re = 50$, 100, 250, 500, 750, 1000, 1250, 1500, 1750 and 2000. The value of $\bar{C}_T$ increases from negative to positive when *St* and *Re* are increased, where $\bar{C}_T < 0$ emerges at smaller *Re* and/or *St*, and $\bar{C}_T > 0$ is observed at larger *Re* and/or *St*, with the solid line ($\bar{C}_T = 0$) representing the drag–thrust boundary. Compared with the travelling wavy motion (figure 4), the pitching motion ($\lambda = 1000 \to \infty$) produces a higher $\bar{C}_T$ with the drag–thrust boundary ($\bar{C}_T = 0$) shifting to a smaller *Re* and *St*.

Figure 10 displays C_T histories in one oscillation period at four selected points: A ($St = 0.2$, $Re = 100$) in drag regime, B ($St = 0.4$, $Re = 250$) close to the drag–thrust boundary at high λ, C ($St = 0.6$, $Re = 600$) close to the drag–thrust boundary at small λ and D ($St = 0.8$, $Re = 1000$) in thrust regime, all marked in the *St*-*Re* map (figure 4). Similar to the previous works on the pitching foil (Koochesfahani 1989), two C_T peaks are observed in the upstroke and downstroke. The travelling wavy foil experiences drag during the entire period at $St = 0.2$, $Re = 100$ (figure 10*a*). For the given *St* and *Re*, the C_T peak becomes larger when λ increases from 0.50 to 2.0. At intermediate *St* and *Re* values (points B and C), the foil undergoes both drag and thrust in the period (figure 10*b*,*c*). On the other hand, at a higher *St* and *Re*, only thrust acts on the foil in the entire period (figure 10*d*). The C_T amplitude (the gap between maximum and minimum) grows with increasing *St*, *Re* and λ (figure 10*a*–*d*). A smaller λ, therefore, engenders a more steady thrust, which explains the swimming behaviour of the *anguilliform* swimmer. On the other hand, the maximum instantaneous thrust generated for a higher λ explicates why the slender swimmer usually employs the C-start strategy during the survival behaviour (Gazzola *et al.* 2012). More discussion on the instantaneous thrust coefficient is provided in Appendix A.3.

The total thrust acting on the travelling wavy foil consists of a friction drag (negative thrust) and a form thrust (positive or negative), i.e. $C_T = C_{Tp} + C_{Tf}$, where C_{Tp} and C_{Tf} denote the instantaneous pressure and friction thrust coefficients, respectively. Naturally, $\bar{C}_T = \bar{C}_{Tp} + \bar{C}_{Tf}$. Figure 11 shows the dependence of $\bar{C}_{Tp}$, $\bar{C}_{Tf}$ and $\bar{C}_T$ on *St* and *Re*. At a moderate *Re* of 1000, the dependence of $\bar{C}_{Tp}$, $\bar{C}_{Tf}$ and $\bar{C}_T$ on $St = 0.1$–1.0 and $\lambda = 0.5$–2.0 is illustrated in figure 11(*a*). With increasing *St*, $\bar{C}_{Tp}$ grows from negative to positive while $\bar{C}_{Tf}$ remains negative and linearly decreases, regardless of λ (figure 11*a*). To understand the dependence of $\bar{C}_{Tp}$ and $\bar{C}_{Tf}$ on *St*, we made polynomial fit to the curves as $\bar{C}_{Tp} = c_{0p} + c_{1p}St + c_{2p}St^2 + c_{3p}St^3$ and $\bar{C}_{Tf} = c_{0f} + c_{1f}St$. The curve fitting provided $c_{2p} \approx 0.001 \approx 0$ regardless of λ while c_{1p} and c_{1f} were almost equal in magnitude but opposite in sign.

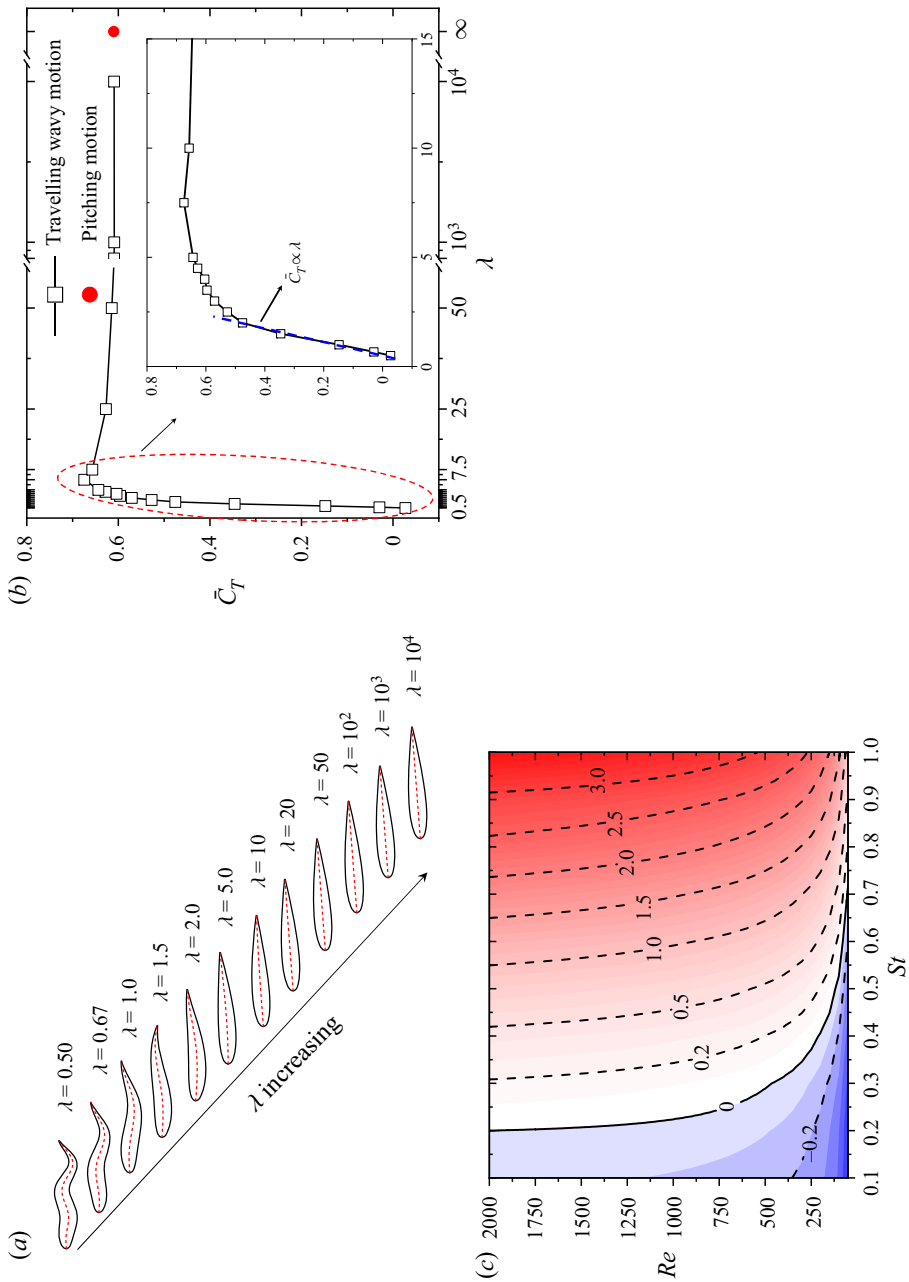

Figure 9. (*a*) Change of foil shape with increasing λ; (*b*) dependence of $\bar{C}_T$ on λ at $a_1 = 0.05$, $St = 0.5$ and $Re = 1000$; the blue-dashed line in the inset represents the linearity; (*c*) $\bar{C}_T$ contours in the St–Re plane at $a_1 = 0.05$, $\lambda = 1000$, where the black solid line denotes the drag–thrust boundary.

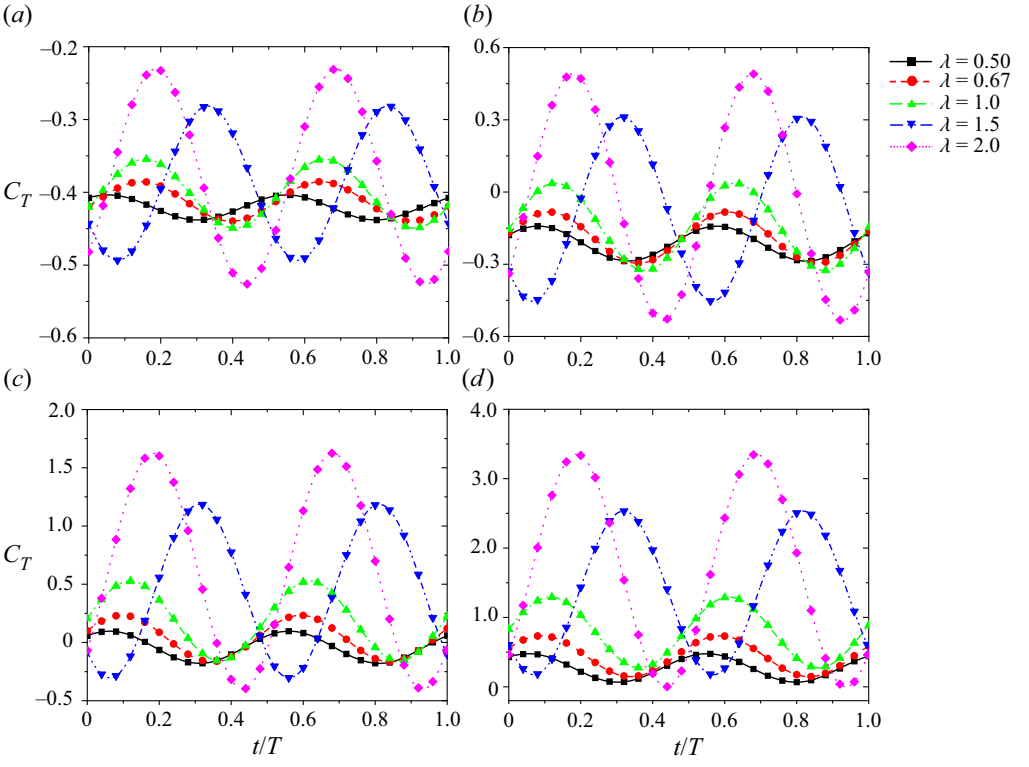

Figure 10. The instantaneous thrust coefficient for the travelling wavy foil in one oscillation period. In (*a*), $\bar{C}_T = -0.423$, -0.416, -0.407, -0.392 and -0.386 for $\lambda = 0.50$, 0.67, 1.0, 1.5 and 2.0, respectively; in (*b*), $\bar{C}_T = -0.212$, -0.185, -0.176, -0.101 and -0.052 for $\lambda = 0.50$, 0.67, 1.0, 1.5 and 2.0, respectively; in (*c*), $\bar{C}_T = -0.026$, 0.056, 0.207, 0.468 and 0.637 for $\lambda = 0.50$, 0.67, 1.0, 1.5 and 2.0, respectively; and in (*d*), $\bar{C}_T = 0.230$, 0.402, 0.746, 1.311 and 1.687 for $\lambda = 0.50$, 0.67, 1.0, 1.5 and 2.0, respectively. (*a*) $St = 0.2$, $Re = 100$, (*b*) $St = 0.4$, $Re = 250$, (*c*) $St = 0.6$, $Re = 500$ and (*d*) $St = 0.8$, $Re = 1000$.

The total thrust can, therefore, be written as $\bar{C}_T = \bar{C}_{Tp} + \bar{C}_{Tf} = (c_{0p} + c_{0f}) + c_{3p}St^3$. For a stationary foil ($St = 0$), $c_{0p} + c_{0f} = \bar{C}_{T0}$, which makes $\bar{C}_T = \bar{C}_{T0} + c_{3p}St^3$. The polynomial fit of $\bar{C}_{Tp}$ and linear fit of $\bar{C}_{Tf}$ are presented in figure 11(*a*), where the data derived from different St values collapse well on the lines. When λ increases, $\bar{C}_{Tp}$ rapidly grows while $\bar{C}_{Tf}$ does not significantly change. That is, the effect of λ on $\bar{C}_T$ is largely determined by $\bar{C}_{Tp}$. Figure 11(*b*) displays the Re effect on $\bar{C}_{Tp}$, $\bar{C}_{Tf}$ and $\bar{C}_T$ at $St = 0.5$ at different λ values. With increasing Re, the magnitude of $\bar{C}_{Tf}$ (negative in the entire range of Re) diminishes rapidly at $Re \leq 500$ but mildly at $Re > 500$. In other words, $\bar{C}_{Tf}$ is more sensitive to Re for $Re \leq 500$ than for $Re > 500$. On the other hand, the reduction of $\bar{C}_{Tp}$ at $Re \leq 500$ is not as much as that of the $\bar{C}_{Tf}$ magnitude, $\bar{C}_{Tp}$ remaining more or less constant at $Re > 500$. As such, $\bar{C}_T$ grows more rapidly at $Re \leq 500$ than at $Re > 500$. Again, with increasing λ, the $\bar{C}_{Tf}$ distribution does not change appreciably while $\bar{C}_{Tp}$ enhances significantly, as does $\bar{C}_T$. The observation conforms with the dependence of $\bar{C}_T$ on Re and λ presented in figure 7.

Figure 12(*a*) shows the distributions of the local time-mean pressure thrust coefficient $\bar{C}^s_{Tp}$ along the foil, where s varying from 0 to L is the distance measured from the

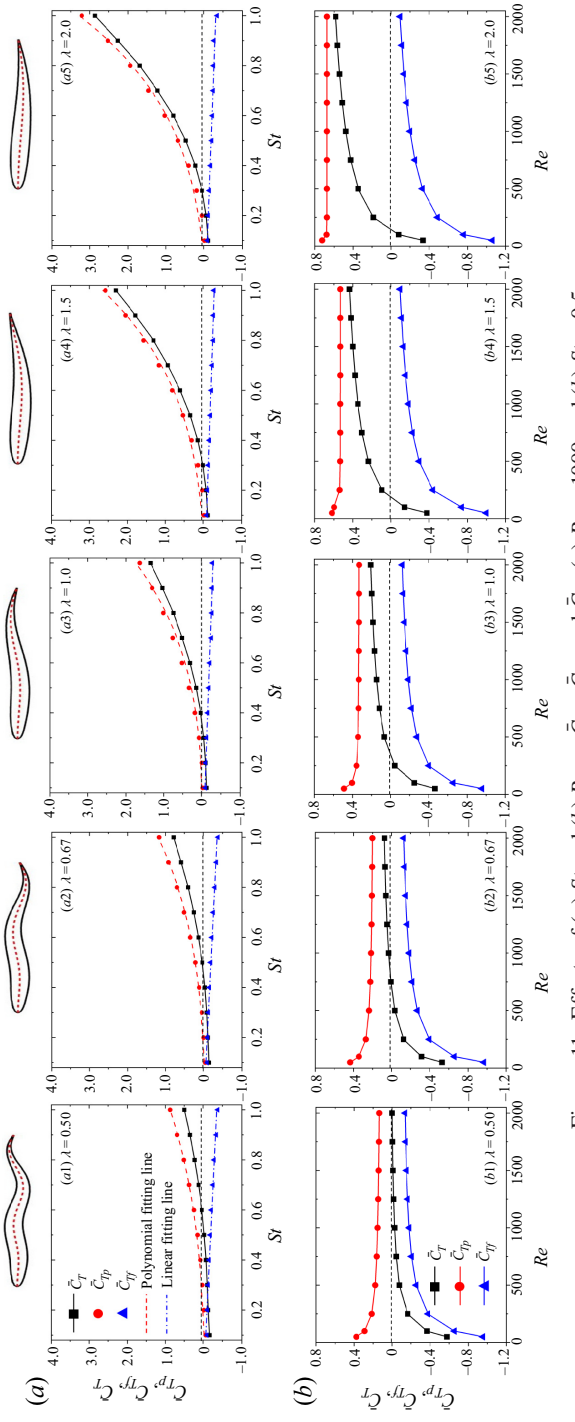

Figure 11. Effects of (*a*) *St* and (*b*) *Re* on $\bar{C}_{Tp}$, $\bar{C}_{Tf}$ and $\bar{C}_T$; (*a*) $Re = 1000$ and (*b*) $St = 0.5$.

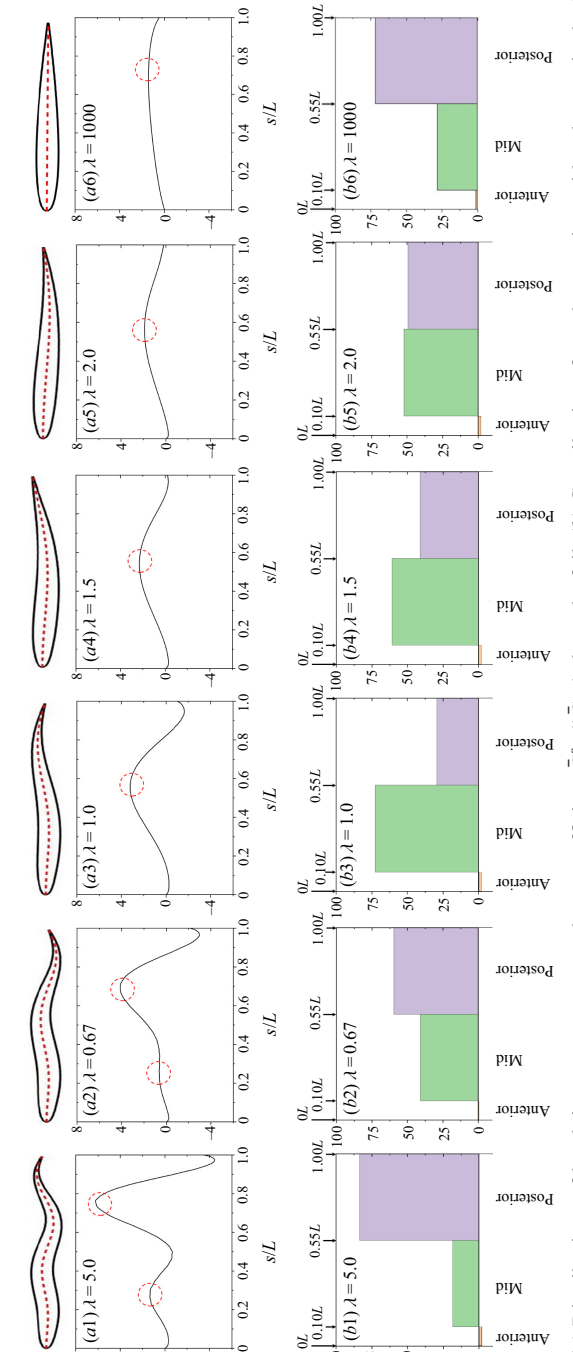

Figure 12. (*a*) Distributions of local time-mean pressure thrust coefficient $\bar{C}^s_{Tp}/|\bar{C}_{Tp}|$ along the foil. (*b*) Contributions from the anterior, mid and posterior bodies on pressure thrust. Here, $(St, Re) = (0.5, 1000)$.

leading edge. As expected, $\bar{C}^s_{Tp}/|\bar{C}_{Tp}|$ is negative near the leading edge for $\lambda \leq 2.0$ (figure 12*a*1–*a*5). As marked by the red-dashed circles for $\lambda = 0.50$ (figure 12*a*1), there are two $\bar{C}^s_{Tp}/|\bar{C}_{Tp}|$ peaks at $s/L = 0.26$ and 0.76, the latter being 4.6 times higher than the former. The trailing edge ($s/L = 0.90$–1.00) largely undergoes negative thrust while the positive thrust is largely generated at $0.55 < s/L < 0.90$. With increasing λ from 0.5 to 2.0 (figure 12*a*1–*a*5), (i) $\bar{C}^s_{Tp}/|\bar{C}_{Tp}|$ near the leading edge does not change appreciably, remaining negative for $s/L < 0.07$–0.14 depending on λ, (ii) the first peak weakens, losing its identity for $\lambda \geq 1.0$, (iii) the second peak shifts toward the middle, becoming wider and blunt and (iv) the negative thrust near the trailing edge reduces in magnitude, becoming positive at $\lambda = 2.0$. Figure 12(*a*6) shows the $\bar{C}^s_{Tp}/|\bar{C}_{Tp}|$ distribution at $\lambda = \infty$ to understand the trend for the widely studied pitching foil. The trend $\bar{C}^s_{Tp}/|\bar{C}_{Tp}| > 0$ emerges at all s/L values. When λ increases from 2.0 to ∞, the peak $\bar{C}^s_{Tp}/|\bar{C}_{Tp}|$ is further postponed from $s/L = 0.55$ to 0.69, with the peak magnitude declining from 1.90 to 1.42.

From the $\bar{C}^s_{Tp}/|\bar{C}_{Tp}|$ distributions (figure 12*a*), it is worth seeing the contributions of anterior, mid and posterior bodies to pressure thrust. Following Lucas, Lauder & Tytell (2020), we define the anterior, mid and posterior bodies as $0.00 \leq s/L \leq 0.10$, $0.10 < s/L \leq 0.55$ and $0.55 < s/L \leq 1.00$, respectively. The contributions δ_p of the three portions to pressure thrust are estimated as

$$\delta_p = \begin{cases} \dfrac{\int_{0.00}^{0.10} \bar{C}^s_{Tp}\, \mathrm{d}(s/L)}{\bar{C}_{Tp}} & \text{for anterior body} \\ \dfrac{\int_{0.10}^{0.55} \bar{C}^s_{Tp}\, \mathrm{d}(s/L)}{\bar{C}_{Tp}} & \text{for mid body} \\ \dfrac{\int_{0.55}^{1.00} \bar{C}^s_{Tp}\, \mathrm{d}(s/L)}{\bar{C}_{Tp}} & \text{for posterior body} \end{cases} . \tag{3.5}$$

The corresponding results are presented in figure 12(*b*). The anterior body provides a negative contribution ($\delta_p < 0$), small in magnitude, to the pressure thrust for all λ values. With increasing λ, δ_p for the mid body firstly increases for $0.50 \leq \lambda \leq 1.0$ and then declines for $1.0 \leq \lambda \leq 2.0$, while the posterior body shows an opposite scenario. In other words, the posterior body provides the largest $\delta_p = 83.18\,\%$ at the smallest $\lambda = 0.50$ examined, and the mid body renders the greatest $\delta_p = 72.76\,\%$ at $\lambda = 1.0$. Their contributions are comparable at the largest $\lambda = 2.0$ examined. At $\lambda = \infty$ (figure 12*b*6), δ_p for the mid body shrinks while that for the posterior body grows to 55 %, a 12 % increase from $\lambda = 2.0$. This result conforms to the previous works on the pitching foil (e.g. Das *et al.* 2016; Alam & Muhammad 2020) as well as the biological observations (Lucas *et al.* 2020). In particular, Alam & Muhammad (2020) showed that the pressure field over the pitching foil characterizes the inertial effects and determines the thrust generation. The observations suggest that for the *anguilliform* swimmers with a smaller λ (e.g. the eel, Lindsey 1978), the pressure thrust is mainly generated from the posterior oscillation, while both mid and posterior are equally important to generate pressure thrust for the *carangiform* (e.g. mackerel, Lindsey 1978) and *thunniform* swimmers (e.g. tuna, Lindsey 1978) with $\lambda > 1.0$.

Figure 13(*a*) shows local time-mean friction thrust $\bar{C}^s_{Tf}$ distributions along the foil. The entire foil undergoes negative $\bar{C}^s_{Tf}$. In the anterior region, the $\bar{C}^s_{Tf}/|\bar{C}_{Tf}|$ plummets immediately behind the leading edge and then grows rapidly. The increase in $\bar{C}^s_{Tf}/|\bar{C}_{Tf}|$ is rather mild in the mid region while the second half of the posterior region has a decreasing

$\bar{C}^s_{Tf}/|\bar{C}_{Tf}|$. Interestingly, the minimum $\bar{C}^s_{Tf}/|\bar{C}_{Tf}|$ in the anterior region rises with increasing λ while that in the posterior region drops. The influence of λ on $\bar{C}^s_{Tf}/|\bar{C}_{Tf}|$ is less in the mid region than in the other two regions. With λ increasing from 2.0 to ∞, $\bar{C}^s_{Tf}/|\bar{C}_{Tf}|$ magnitudes at the leading and trailing edges become smaller and larger, respectively. A native swimmer uses lateral lines as sensors to achieve the flow information (e.g. pressure and shear stress around itself) and hence to make a swimming decision, while the lateral lines are mainly distributed at the head and caudal fin of a fish (Sapède *et al.* 2002). Recently, Verma *et al.* (2020) studied optimal sensor configurations that enable swimmers to maximize the information gathered from their surrounding flow field. At $\lambda \approx 1.0$, it is noted that the shear stress sensors should be densely distributed in the anterior and in the second half of the posterior regions of the swimmer.

Similar to the definition of δ_p in (3.6), we employed δ_f to denote the contributions of anterior, mid and posterior bodies to the friction thrust. When λ grows from 0.50 to 2.0, figure 13(*b*) depicts that the δ_f decreases from 28.05 % to 21.71 % for the anterior body and from 43.44 % to 32.92 % for the mid body, while increasing from 28.51 % to 45.37 % for the posterior body. For $\lambda \leq 2.0$, $\delta_f > 20$ % for the anterior, mid and posterior regions, which suggests that the contributions from all portions are significant. The increase in λ from 2 to ∞ leads to declining δ_f for the anterior and mid bodies but increasing δ_f for the posterior body. At $\lambda = \infty$, the posterior body undergoes $\delta_f = 50.24$, an 11 % increase from $\lambda = 2$, which suggests that the posterior body is the main contributor to the friction drag.

3.2. *Dependence of added mass, added damping and efficiency on Re, St and λ*

For the undulating swimmer, the added mass plays a dominant role in the propulsive performance (Lighthill 1970, Candelier, Boyer & Leroyer 2011, Eloy, 2012, Paniccia *et al.* 2021). In the elongated-body theory (Lighthill 1970), the added mass per unit length at the foil trailing edge can be calculated from a curvilinear coordinate system as $\rho\pi h^2/4$, where h denotes the thickness of the foil and is assumed to be smaller enough, i.e. $h \ll L$. As Lighthill's theory is inviscid, the viscous influence is neglected, while recent work reveals that the resistive mechanism is also crucial for the inertial undulatory swimmers (Piñeirua, Godoy-Diana & Thiria 2015). Both h/L and Re effects cannot be ignored in the case of viscous flow. It is thus worth understanding how the added mass is affected by St, Re and λ and how it impacts the thrust and power.

Generally, the total fluid added mass m_a due to the foil oscillation can be calculated as

$$m_a = \int_0^{L_s} m_x \, \mathrm{d}x, \tag{3.6}$$

where x is measured from the leading edge and m_x denotes the added mass for an elemental length dx (figure 14*a*). A summation can be considered to replace the integral in (3.6), i.e.

$$m_a = \sum_{n=1}^{n=N} m_n, \tag{3.7}$$

where n is the number of sample slices of the foil. The difference in the estimated m_a between $N = 20$ and 30 is found to be less than 1 %. The value $N = 20$ is adopted (figure 14*a*). Each slice is assumed to be sinusoidally oscillating in the vertical direction. Thus, m_n can be calculated using the equation introduced by Qin, Alam & Zhou (2017) for

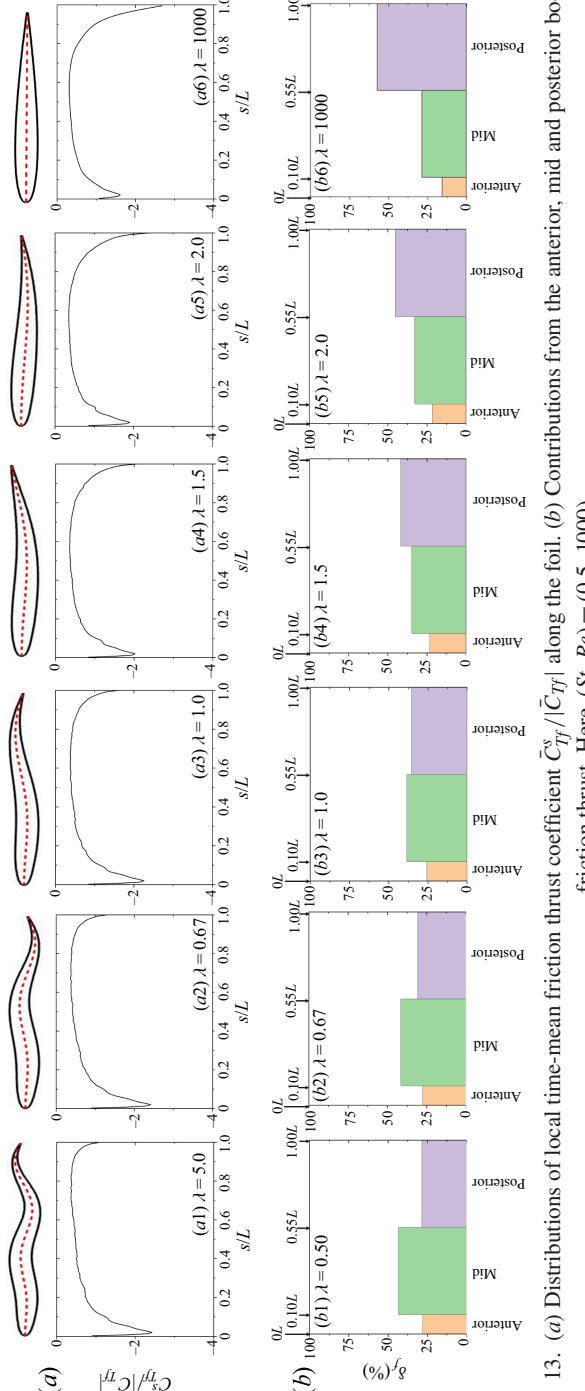

Figure 13. (*a*) Distributions of local time-mean friction thrust coefficient $\bar{C}^s_{Tf}/|\bar{C}_{Tf}|$ along the foil. (*b*) Contributions from the anterior, mid and posterior bodies on friction thrust. Here, $(St, Re) = (0.5, 1000)$.

an oscillating cylinder, as

$$m_n = \frac{F_{Ln}\cos\phi}{\omega^2 Y_n}, \tag{3.8}$$

where F_{Ln} is the amplitude of the time-dependent lift force $F_L(t) = F_{Ln}\sin(\omega t + \phi)$ at slice n, Y_n is the amplitude of the displacement of slice n with $Y(t) = Y_n \sin(\omega t)$, ϕ is the phase shift between $F_L(t)$ and $Y(t)$ and $\omega = 2\pi/T$. Note that the m_n is the effective added mass, not the potential added mass (Williamson & Govardhan 2004). The added mass ratio m_a^* can then be estimated as

$$m_a^* = \frac{m_a}{m_f}, \tag{3.9}$$

where m_f is the mass of fluid displaced by the foil. In our paper, the effective added mass is calculated from the component of the fluid force in phase with the foil acceleration ((3.7)–(3.9)). The effective added mass includes both potential added mass and flow-induced added mass (Konstantinidis, Dorogi & Baranyi 2021; Alam 2022). As a result, the effective added mass can be positive or negative, as shown in figure 14(*b*1). More discussion on the relationship between the effective added mass and potential added mass can be found in Facchinetti, de Langre & Biolley (2004) and Han & de Langre (2022).

How m_a^* is contingent on St and Re is illustrated in figure 14(*b*). When $Re = 1000$ (figure 14*b*1), m_a^* is negative at $St = 0.1$, and its magnitude gets large with increasing λ. On the other hand, m_a^* is positive at $St \geq 0.2$, increasing with increasing St and λ. Note that a negative m_a^* makes the foil lighter to move, while a positive m_a^* makes the foil heavier. The value of m_a^* is a stronger function of St at a larger λ. The effect of Re on m_a^* can be understood from figure 14(*b*2), where m_a^* declines with increasing in Re, particularly at $Re \leq 500$, regardless of λ. The viscous effect on m_a^* becomes negligible when Re is sufficiently large. On the other hand, λ has a strong influence on m_a^*, the higher the λ, the larger the m_a^*.

The effect of St, Re and λ on the out-of-phase component of the lift force (i.e. added damping) is also considered. Recalling the work of Qin *et al.* (2017), the added damping of the travelling wavy foil can be defined as

$$c_a = \sum_{n=1}^{n=N} c_n, \tag{3.10}$$

where

$$c_n = -\frac{F_{Ln}\sin\phi}{\omega Y_n}. \tag{3.11}$$

As shown in figure 14(*c*), St and Re have effects on c_a, where c_a reduces with increasing St and/or Re, and $c_a < 0$ at $St = 0.5$ for all tested Re values. The case $c_a > 0$ is only observed at $\lambda = 0.50$, 0.67 and 1.0 with $St = 0.1$ (figure 14*c*1). The declination of c_a with increasing St is larger at a larger λ (figure 14*c*1). As such, the larger the St, the greater the c_a decrease with increasing λ. Since a negative c_a implies the flow assisting the motion, the contribution by the flow is constructive to $\bar{C}_T$ when St, Re and λ all are increased (figure 4).

The effect of St and Re on the input power $\bar{C}_{pi}$ required to move the foil is depicted in figure 14(*d*). The total power is composed of power P_s associated with oscillation and power P_T associated with thrust (Shen *et al.* 2003; Dong & Lu 2005). The former is

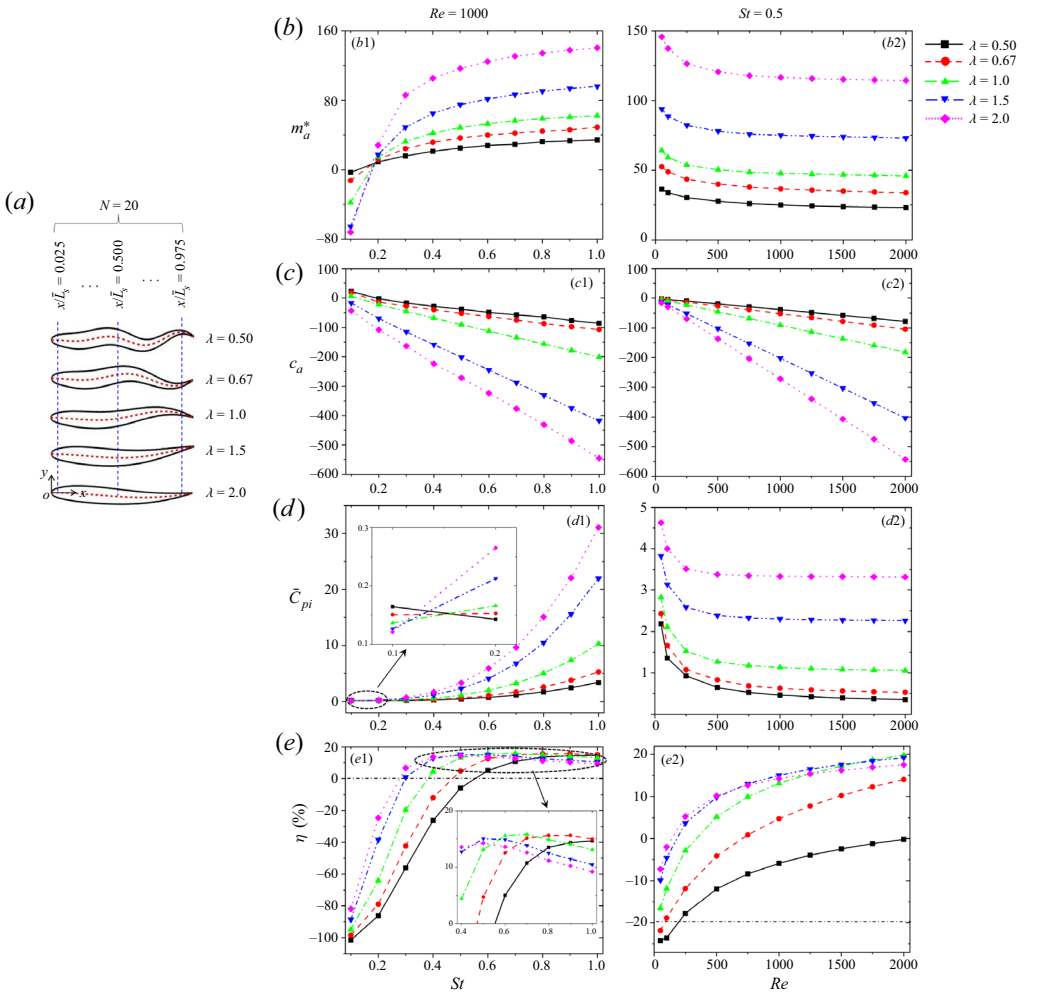

Figure 14. (*a*) Sketches for the sampling slices. Effects of *St*, *Re* and λ on (*b*) m_a^*, (*c*) c_a, (*d*) $\bar{C}_{pi}$ and (*e*) η. Here, (*b*1, *c*1, *d*1, *e*1) $Re = 1000$, and (*b*2, *c*2, *d*2, *e*2) $St = 0.5$.

required to produce the lateral oscillations of the foil while the latter is needed to generate the thrust force. The mathematical definitions of P_s and P_T are as follows:

$$P_s = -\oint (f_y^p + f_y^f)[1 + (1 + \mathrm{d}y/\mathrm{d}t)^2]^{1/2} \frac{\mathrm{d}y}{\mathrm{d}t}\, \mathrm{d}x, \tag{3.12}$$

and

$$P_T = -F_x(t)U, \tag{3.13}$$

where $\oint$ denotes the integration along the foil surface, $f_y^p = -p$ and $f_y^f = \mu[2(\partial v/\partial y) - (\mathrm{d}y/\mathrm{d}x)(\partial v/\partial x + \partial u/\partial y)]$ with u and v representing the velocity components in the x and y directions, respectively. Thus, time-mean power coefficient $\bar{C}_{pi}$ in one oscillation period is defined as

$$\bar{C}_{pi} = \frac{1}{T}\int_t^{t+T} \frac{P_s + P_T}{0.5\rho U^3 L}\, \mathrm{d}t. \tag{3.14}$$

As illustrated in figure 14(*d*1), $\bar{C}_{pi}$ exponentially grows with increasing St, approximately following $\bar{C}_{pi} \propto St^3$. Alam & Muhammad (2020) mathematically showed that the input power of a pitching foil is highly sensitive to St and varies as the cube of St. For a given St, a larger $\bar{C}_{pi}$ is required for a larger λ for $St \geq 0.2$ while $\bar{C}_{pi}$ deceases with increasing λ at $St = 0.1$ (inset of figure 14*d*1), which coincides with the relationship of m_a^* with λ (figure 14*b*). The $\bar{C}_T$ scaling in (3.4) echoes that $\bar{C}_T$ values at $St = 0.1$ for different λ values are close to each other, with only a 2.36 % difference in $\bar{C}_T$ between $\lambda = 0.50$ and 2.0. As such, P_s is the dominant factor contributing to $\bar{C}_{pi}$. A shorter λ, therefore, causes a higher $\bar{C}_{pi}$ at $St = 0.1$ (see the inset of figure 14*d*1). When $St \geq 0.2$, P_T gradually dominates P_s where a longer λ complements a larger $\bar{C}_T$ (figure 4). It should be noted that $St \geq 0.5$ (depending on λ) provides positive $\bar{C}_T$ (figure 11*a*), hence aquatic animals may use $St \geq 0.5$. The relationship of $\bar{C}_{pi}$ with Re (figure 14*d*2) is similar to that of m_a^* with Re (figure 14*b*2). Overall, a large λ corresponds to a larger m_a^* and a higher $\bar{C}_{pi}$ for $St \geq 0.2$. The dependence of m_a^* on λ evokes that a slender tail or a slender swimming body cannot have a large λ because a large m_a^* makes the tail or body heavier, so it is difficult for the animal to oscillate its tail/body, given that it has limited strength and limited rigidity of the tail. It could thus be said that a longer tail/body may adopt a shorter λ. For example, the λ employed by eel swimmers is shorter than that used by trout (Webb 1984). Biological observations of Gray (1933) provided similar conclusions.

It is also worth investigating how the propulsive efficiency is affected by St, Re and λ. Here, the foil's propulsive efficiency is calculated via

$$\eta = \bar{C}_T / \bar{C}_{pi}. \tag{3.15}$$

Using $\bar{C}_T$ data in figure 11 and $\bar{C}_{pi}$ data in figure 14(*d*), we obtained the relationship of η with St, Re and λ in figure 14(*e*). Following the sign of $\bar{C}_T$ in figure 11(*a*), $\eta < 0$ at a smaller St (figure 14*e*1). When St passes the drag–thrust boundary (3.4), i.e. $St > 2.57Re^{-0.27}\lambda^{-1/3}$, the foil can generate positive thrust ($\bar{C}_T > 0$) (figure 11*a*) and thus a positive efficiency (figure 14*e*1). The value of η increases for a certain range of St, reaching a maximum before declining, except for $\lambda = 0.50$ where η keeps increasing with St up to $St = 1.0$. While the maximum efficiency value is weakly dependent on λ, the St value corresponding to the maximum efficiency is smaller at a larger λ, i.e. $\eta = 14.67\,\%$ for $(St,\ \lambda) = (1.0,\ 0.50)$, $\eta = 15.63\,\%$ for $(St,\ \lambda) = (0.9,\ 0.67)$, $\eta = 15.87\,\%$ for $(St,\ \lambda) = (0.8,\ 1.0)$, $\eta = 15.03\,\%$ for $(St,\ \lambda) = (0.5,\ 1.5)$ and $\eta = 14.26\,\%$ for $(St,\ \lambda) = (0.5,\ 2.0)$, see inset of figure 14(*e*1). The data indicate that $\lambda = 1.0$ renders the largest η. That is, the aquatic swimmers can achieve a higher propulsive efficiency by employing $\lambda \approx 1.0$, which is in agreement with the biological observations from swimming fish (Videler 1993). Figure 14(*e*2) shows the effect of Re on η, where η increases with Re. At $50 < Re \leq 500$, a larger λ leads to a higher η, while $\lambda = 1.5$ and 1.0 cause the higher η at $750 < Re \leq 1500$ and $1750 < Re \leq 2000$, respectively.

Besides the effects of St, Re and λ on m_a^*, it is also worth understanding the distribution of m_n along the foil length, i.e. $n = 1$ - 20. Here, m_n is normalized as $m_n^* = m_n/m_f$. As shown in figure 15, m_n^* is highly dependent on n for large λ ($\geq$ 1.0) values, where it is large (positive) near the midspan ($n = 7$ - 15) and negative near the leading edge of the foil. At small $\lambda = 0.50$ and 0.67 each, m_n^* displays small peaks at $n = 4$ and 17.

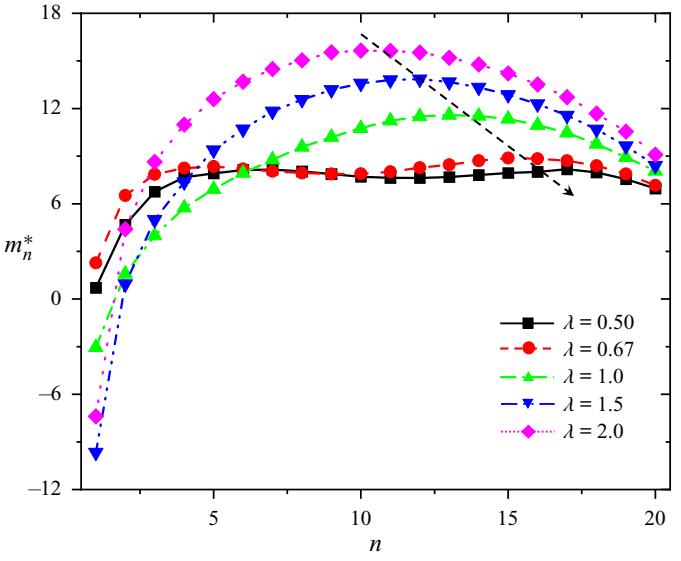

Figure 15. The m_n^* at different slices; $St = 0.5$ and $Re = 1000$.

3.3. *Flow structures*

Following the above discussion on thrust generation, the associated flow structures are presented to gain the physical insight into fluid dynamics around the swimmer. Seven distinguished wake structures are identified in the *St–Re* domain examined: steady wake (+ symbol), quasi Kármán vortex (q-KV) wake (⬠ symbol), quasi reverse Kármán vortex (q-RKV) wake (☆ symbol), KV wake (○ symbol), 2S (two single) aligned wake (■ symbol), RKV wake (δ symbol) and slanted reverse Kármán vortex (s-RKV) wake (∇ symbol). The representative flow structures and their presence in the *St–Re* domain are shown in figures 16 and 17. The steady wake is observed at $St \leq 0.6$ and $Re \leq 250$ (figures 16*a* and 17), where the wake is steady, similar to the flow structure behind a quiescent foil ($St = 0$). With a little increase in *St* and/or *Re*, the steady wake transmutes to q-KV wake (figure 16*b*) or q-RKV wake (figure 16*c*) representing a transition from a steady wake to a classical KV or RKV wake. The q-KV and q-RKV wakes form at low and high *St*, respectively, the former prevailing for smaller λ ($\leq$1.0) only (figure 17). Here, Kármán or reverse Kármán vortices form immediately behind the foil, vanishing rapidly to generate a steady wake downstream (figure 16*a–c*). The generation of a steady wake followed by a Kármán wake was also found in the wake of a fixed elliptical cylinder at $Re = 100$–150 in Shi, Alam & Bai (2020*a*) and Shi *et al.* (2020*b*). Depending on λ, when *Re* is further increased, a KV wake forms, featuring negative and positive vortices above and below the foil symmetry line correspondingly (figure 16*d*). The 2S aligned wake refers to the case where both positive and negative vortices lie on the symmetric line (figure 16*e*). The 2S aligned wake is considered as the boundary between KV and RKV wakes, and has been extensively discussed in previous works (Godoy-Diana *et al.* 2008, 2009; Marais *et al.* 2012; Deng *et al.* 2015, 2016; Andersen *et al.* 2017; Chao *et al.* 2019; Chao *et al.* 2021*b*). The emergence of the 2S aligned wake at the KV–RKV boundary (red dashed line) precedes the drag–thrust boundary (black solid line) in the *St–Re* map (figure 17). The same is true for a pitching foil (Godoy-Diana *et al.* 2008). With a further increase in *St* and/or *Re*, the RKV wake emerges, where the negative and positive vortices nestle

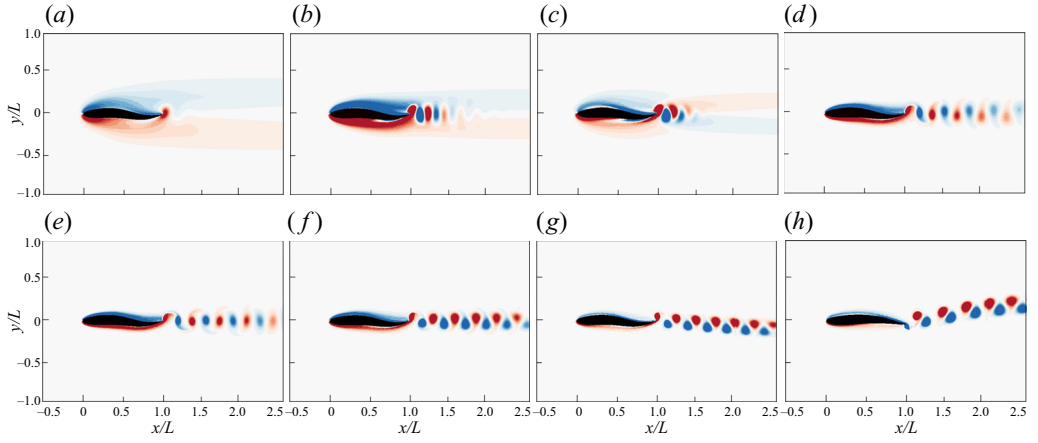

Figure 16. Typical instantaneous vorticity structures: (*a*) steady wake (*St*, *Re*, $\lambda = 0.2$, 100, 1.0); (*b*) q-KV wake (*St*, *Re*, $\lambda = 0.4$, 100, 1.0); (*c*) q-RKV wake (*St*, *Re*, $\lambda = 0.7$, 100, 1.0); (*d*) KV wake (*St*, *Re*, $\lambda = 0.3$, 1000, 1.0); (*e*) 2S aligned wake (*St*, *Re*, $\lambda = 0.3$, 2000, 1.0); (*f*) RKV wake (*St*, *Re*, $\lambda = 0.5$, 1000, 1.0); (*g*) downward slanted reverse Kármán vortex (ds-RKV) wake (*St*, *Re*, $\lambda = 0.8$, 1000, 1.0); and (*h*) upward slanted reverse Kármán vortex (us-RKV) wake (*St*, *Re*, $\lambda = 0.8$, 1000, 1.5).

oppositely to those of KV wake (figure 16*f*). In the s-RKV wake, the symmetric line of two vortex streets does not coincide with the foil symmetric line. The slant direction can be upward or downward. The downward slanted RKV is referred to as the ds-RKV wake (figure 16*g*) while the upward slanted RKV is referred to as the us-RKV wake (figure 16*h*). The slant direction of the s-RKV wake is also affected by λ, see figure 16(*g*,*h*). Generally, the slant direction strongly depends on the first vortex pair generated by the foil (Zheng & Wei 2012). Here, both the ds-RKV and us-RKV wakes are considered as an s-RKV wake because the physical mechanisms of the ds-RKV and us-RKV wakes are identical. The formation of the slanted wake is also common in flow-induced vibrations of cylinders (Bhatt & Alam 2018).

Figure 17 also shows how λ affects the wakes behind a travelling wavy foil, particularly the transition between two different types of flow structures. For example, the KV–RKV wake transition bordered by the 2S aligned wake advances with increasing λ. Similarly, the RKV–s-RKV wake transition (blue dash-dotted line) also shifts to smaller *St* and/or *Re* when λ is increased. In addition, there is no s-RKV wake observed at $\lambda = 0.50$ (figure 17*a*). Physically, λ describes how the foil locomotion propagates from the leading to trailing edges. Therefore, the foil's horizontal acceleration at the trailing edge declines with the decrease in λ. As a result, the convection velocity of the vortices with respect to U also decreases with declining λ. In the previous work, Godoy-Diana *et al.* (2009) showed that the generation of the s-RKV wake is significantly dependent on the value of this convection velocity, where a larger value of this convection velocity may induce an s-RKV wake. A smaller λ thus postpones the transition between RKV and s-RKV wakes.

To evaluate quantitatively the influence of *St*, *Re* and λ on vortex strength in different regimes, figure 18 presents dimensionless spanwise vorticity ω^* ($= \omega L/U$) structures at the four selected points located in the *St*–*Re* plane (figure 17). The value of ω^* increases with *St*, *Re* and λ, which is consistent with the change in $\bar{C}_T$ in figure 4. A similar relationship of the spatial wavelength Δd with *St, Re* and λ is noticeable, having the same correspondence with $\bar{C}_T$. The growth of Δd with *St* and *Re* is ascribed to the increased velocity of vortices

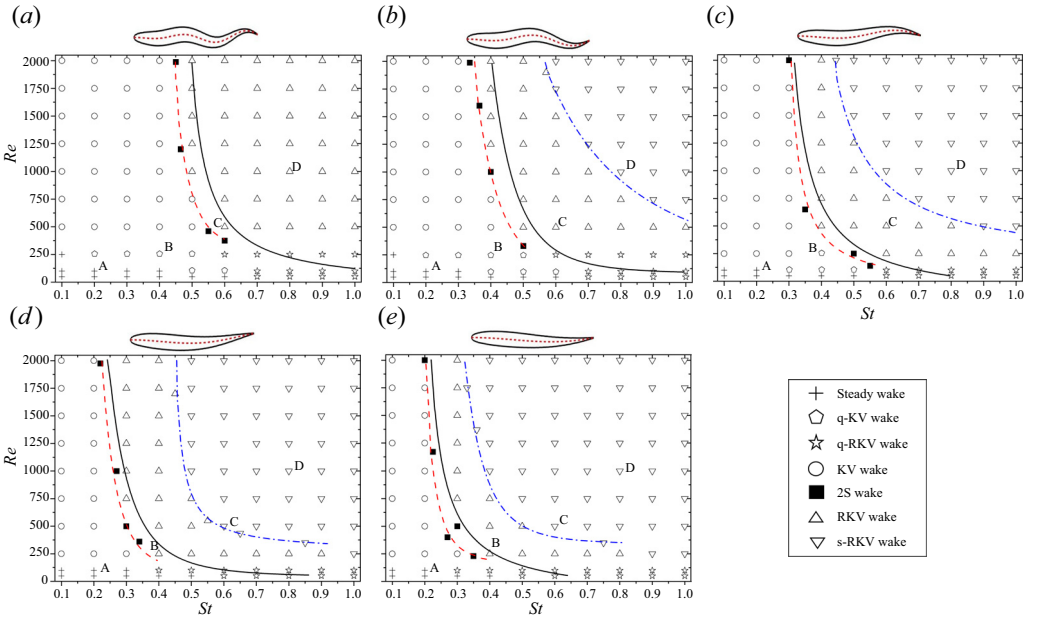

Figure 17. The wake structure map with the black solid line denoting the drag–thrust boundary, red dashed line denoting the KV–RKV wake boundary and blue dash-dotted line denoting the RKV-s-RKV wake boundary. Here, A, B, C and D are four points selected as A ($St = 0.2$, $Re = 100$) in drag regime, B (0.4, 250) close to the drag–thrust boundary at high λ, C (0.6, 600) close to drag-thrust boundary at small λ and D (0.8,1000) in thrust regime to show the influence of λ on flow structures in figure 17. Here, (*a*) $\lambda = 0.50$, (*b*) $\lambda = 0.67$, (*c*) $\lambda = 1.0$, (*d*) $\lambda = 1.5$ and (*e*) $\lambda = 2.0$.

when St and Re are increased. On the other hand, it is easy to understand that a smaller λ would lead to a smaller velocity of the vortices, hence a smaller Δd and $\bar{C}_T$.

Figure 19(*a*) illustrates the effect of St on the wake structure at $Re = 1000$ and $\lambda = 1.0$. A couple of observations can be made here. First, when St is increased, the wake structure transmutes from the KV wake (figure 19*a*1) into the RKV wake (figures 19*a*2 and 19*a*3) and then into the s-RKV wake (figures 19*a*4–19*a*6). Second, the streamwise spatial wavelength of vortices in the vortex street shrinks with increasing St, i.e. vortices are densely distributed for a higher St. Third, an increase in St enhances vorticity magnitudes of vortices in the wake. Based on the definition of the St (2.2), one can understand that the increase in St corresponding to a decrease in the undulating period T causes an increase in acceleration and velocity of the foil tail, and hence results in the enhancement of vorticity (Das *et al.* 2016; Alam & Muhammad 2020; Muhammad, Alam & Noack 2022). Figure 19(*b*) shows how Re affects the wake structures at $St = 0.8$ and $\lambda = 1.0$. When Re is increased, the wake structure modifies from RKV to s-RKV, and vorticity magnitudes rise. Since Re physically describes the fluid resistance, it is easy to understand that ω^* and $\bar{C}_T$ increase when Re increases (figure 4*c*). Also, the slant angle of the RKV wake gradually rises when Re increases from 1000 to 2000, which ties in with the work on a pitching foil by Das *et al.* (2016).

3.4. *Effect of λ on velocity and pressure on the foil*

Figure 20 illustrates the instantaneous relative streamwise velocity $u_r^*(= u/U - 1)$ snapshots at $y/L = 0.15$ (upper side) and -0.15 (lower side), where u denotes the instantaneous streamwise velocity. Three λ values, i.e. $\lambda = 0.50$, 1.0 and 2.0, are presented.

https://doi.org/10.1017/jfm.2022.624 Published online by Cambridge University Press

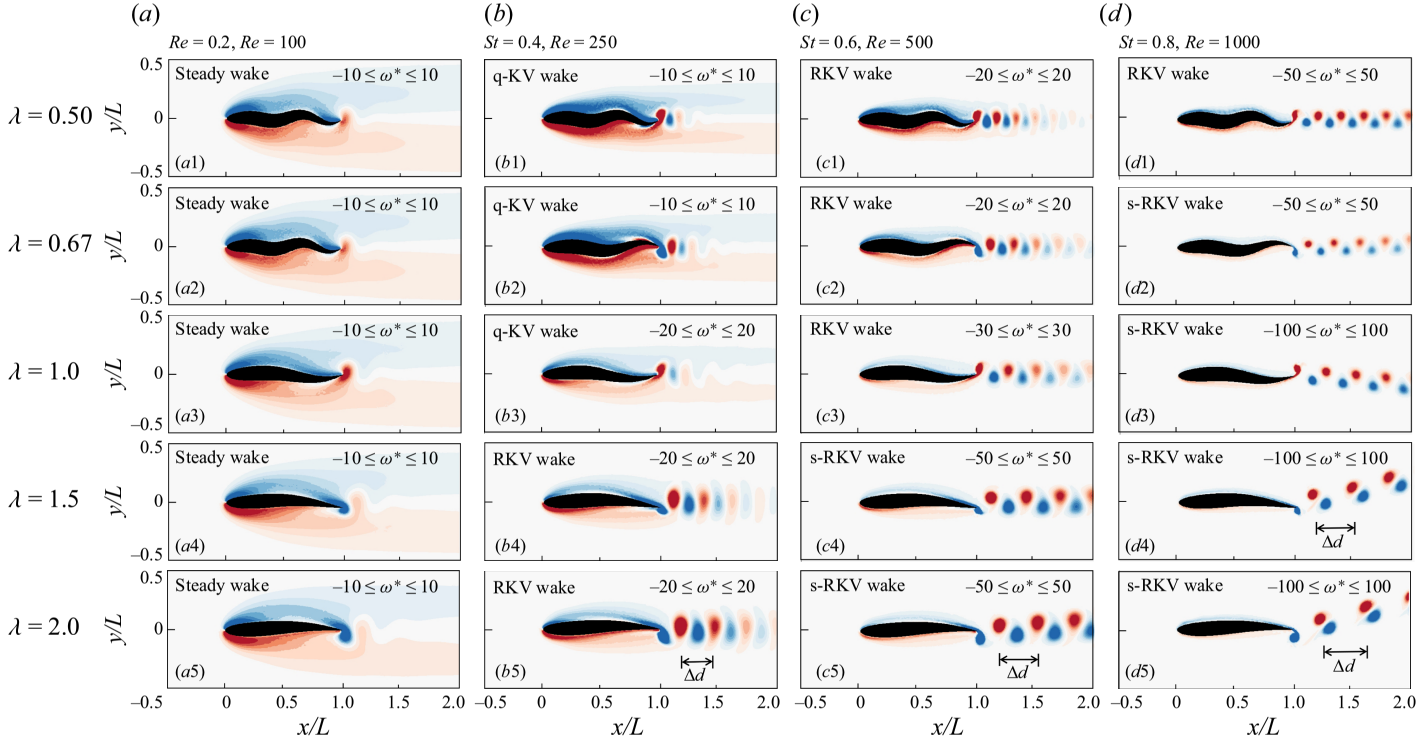

Figure 18. Contours of spanwise vorticity $\omega^* = \omega L/U$. The red and blue colours denote positive and negative ω^*, respectively.

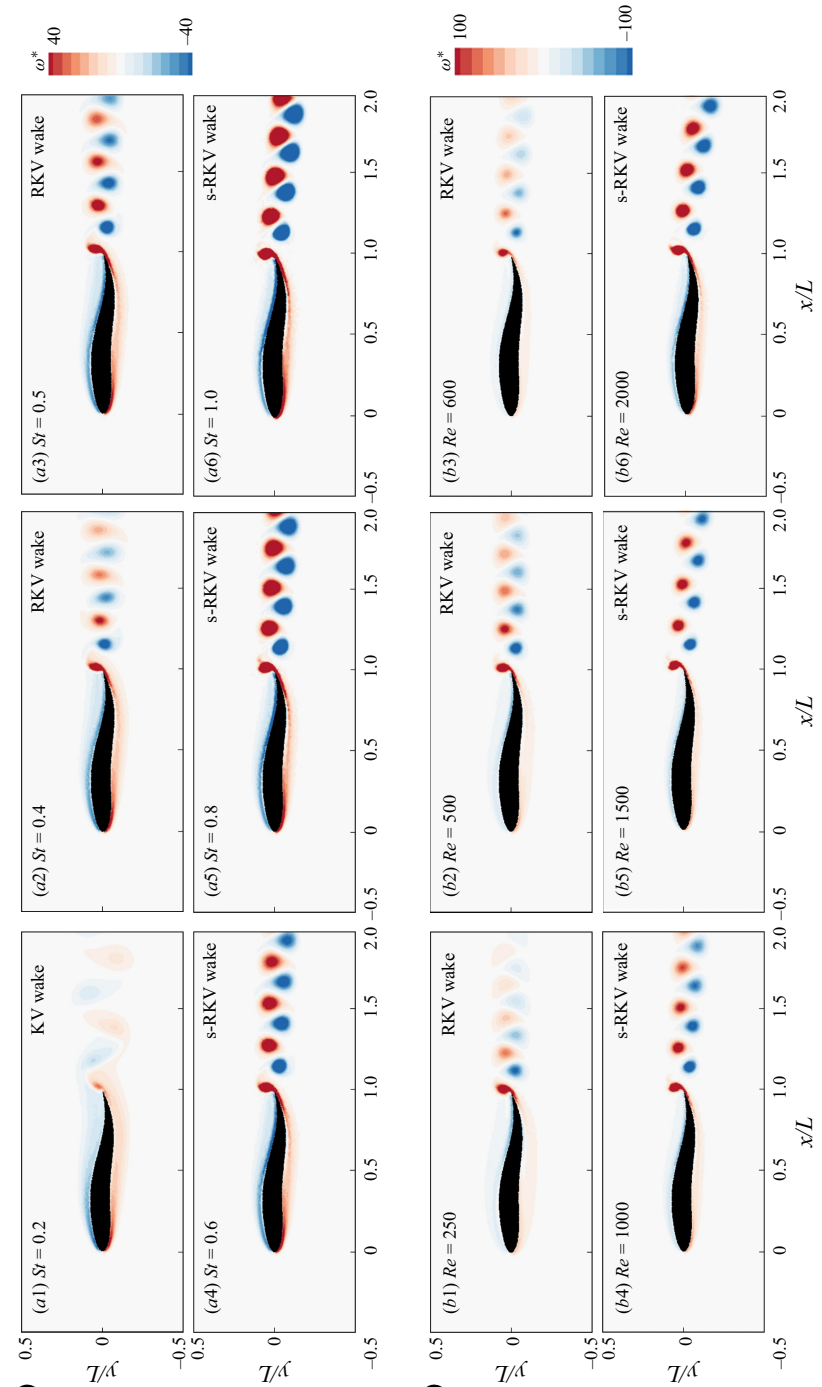

Figure 19. Effects of (*a*) *St* and (*b*) *Re* on flow patterns; (*a*) $Re = 1000$ and (*b*) $St = 0.8$.

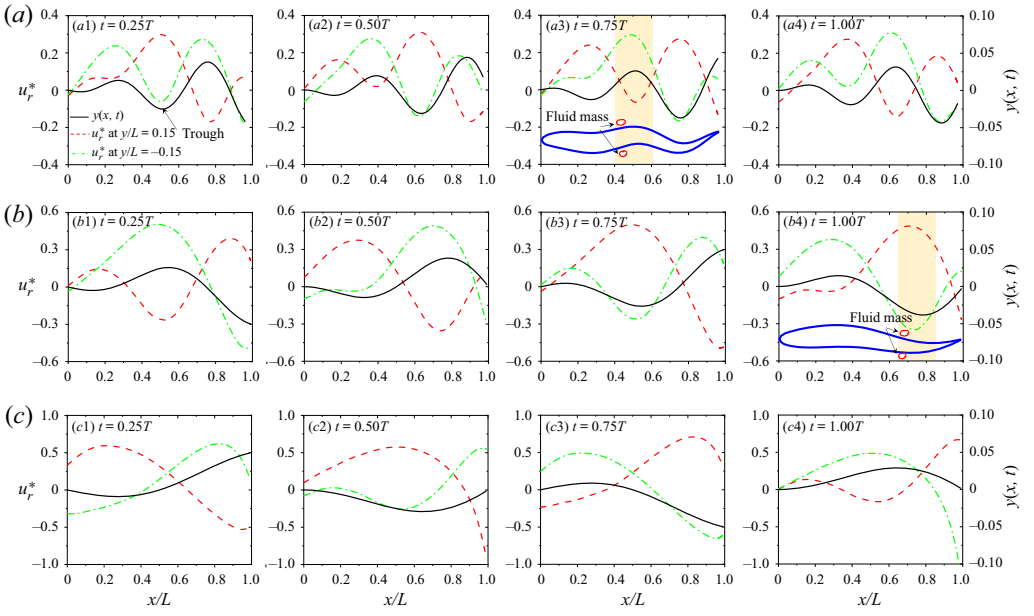

Figure 20. Variation of $u_r^* = (u/U - 1)$ over the foil at $y/L = 0.15$ (red dashed line) and $y/L = -0.15$ (green dash-dotted line), where u is the local instantaneous streamwise velocity. The black solid line denotes the foil centreline profile; $(St, Re) = (0.5, 1000)$ with (*a*) $\lambda = 0.50$, (*b*) $\lambda = 1.0$ and (*c*) $\lambda = 2.0$.

Here u_r^* can be considered as the indicator of local momentum transport in the streamwise direction. It is thus connected to the generation of thrust. It is worth understanding which part of the foil is crucial for generating thrust, particularly when λ is short.

The u_r^* profiles following the foil shape form waves and propagate from the leading edge to the trailing edge. At $y/L = 0.15$ (red dashed line), the peaks in u_r^* occur close to the troughs of the foil wave for a short λ and before the troughs for a long λ. An opposite scenario is observed for the u_r^* profile at $y/L = -0.15$. That is, the travelling of the V-shaped buckets on the upper side and overturned V-shaped buckets on the lower side is mainly responsible for the momentum transport in the streamwise direction in the case of a short λ. On the other hand, for a long λ, both lateral oscillation of foil and streamwise travel of the buckets contribute to the streamwise momentum transport, given that u_r^* peaks precede the troughs.

Consider a slice of the foil (yellow backdrop, figure 20*a*3) forming an overturned V-shaped bucket where a fluid mass over the upper surface of the foil tends to move downstream but is hindered by the crest of the foil. As a result, u_r^* on the upper side is negative, with minimum u_r^* corresponding to the crest of the foil. On the other hand, the fluid mass beneath the lower surface of the foil is pushed downstream by the travelling wave, which results in the increased u_r^*. For a longer λ (figure 20*b*4), each point of the foil's geometry experiences both lateral and horizontal motion. The crests or valleys of the foil shape do not coincide with those of u_r^*.

Figure 21 shows the evolution of the pressure coefficient $C_p = (p - p_\infty)/0.5\rho U^2$ pattern with changing λ at $St = 0.5$ and $Re = 1000$, where p_∞ is the free-stream pressure. The pressure pattern appears complex at $\lambda = 0.50$ (figure 20*a*). With $t/T = 0.25$, the pressure around the crests and troughs (upper side) is negative and positive, respectively, as the crests have downward accelerations and the troughs have upward accelerations (see pointing arrows). The low and high pressure on the crests and troughs increase and their

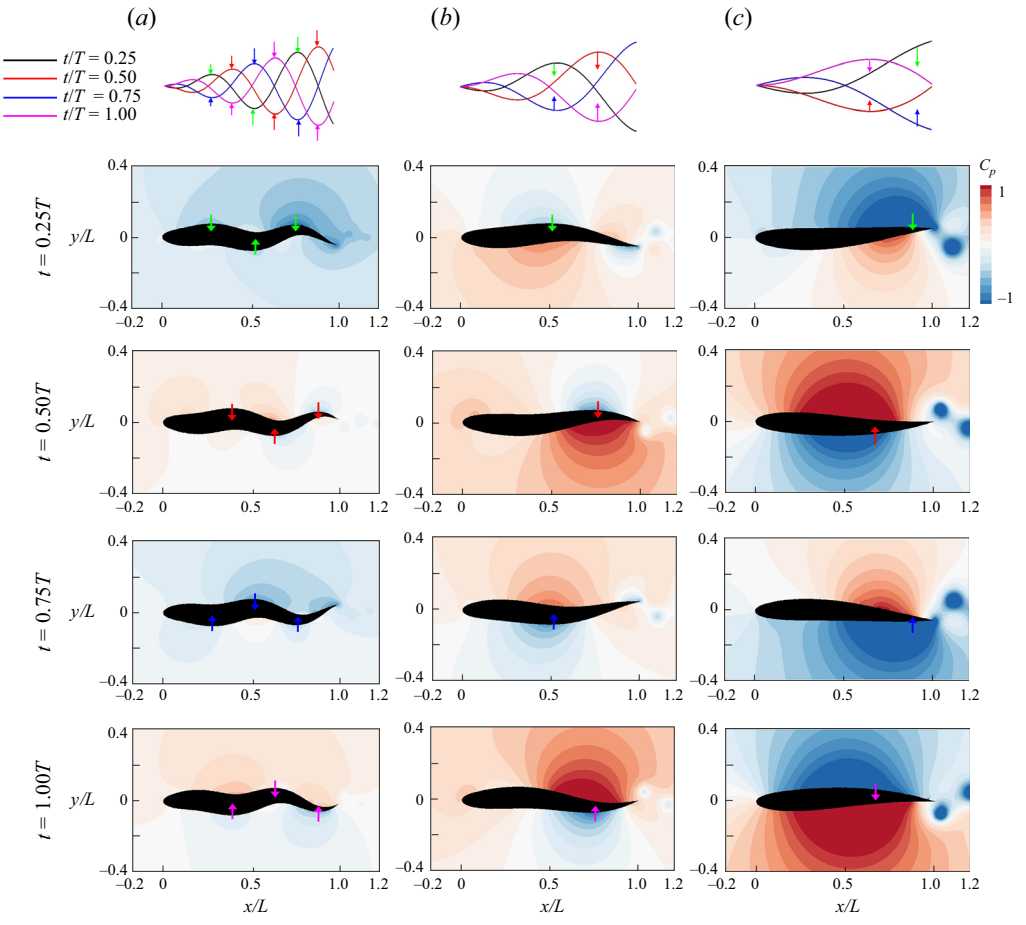

Figure 21. Evolution of pressure coefficient C_p in one undulating period at $St = 0.5$ and $Re = 1000$. The arrows denote the moving direction. (*a*) $\lambda = 0.50$, (*b*) $\lambda = 1.0$ and (*c*) $\lambda = 2.0$.

regions shift downstream from $t/T = 0.25$ to 0.50 following the movement of the foil wave. The pressure is generally larger in the V-shaped or overturned V-shaped buckets than that on other sides (see figures for $t/T = 0.25$–1.0). This explains that the bucket movement in the streamwise direction engenders streamwise momentum transport. Similar observations are made for $\lambda = 1.0$ (figure 21*b*). At $\lambda = 2.0$ (figure 21*c*), when the trailing edge of the foil moves downwards (green arrow) at $t/T = 0.25$, the lower and upper trailing surfaces of the foil undergo high and low pressure, respectively. Since the foil tail is bent upward with its maximum amplitude, the positive and negative pressures appear on the lower and upper trailing surfaces, respectively. At $t/T = 0.50$ where the foil is concave up near the middle (red arrow) with the leading and trailing edges aligned with $y/L = 0$, the pressure is positive on the concave side and negative on the convex side. Naturally, the pressure patterns at $t/T = 0.75$ and 1.0 are opposite to those at $t/T = 0.25$ and 0.50, respectively.

4. Conclusions

A systematic numerical study is performed on the hydrodynamic performance of a fish-like foil undergoing travelling wavy undulation for Strouhal number $St = 0.1$–1.0, Reynolds number $Re = 50$–2000 and non-dimensional wavelength $\lambda = 0.50$–2.0 with the foil length

remaining constant to replicate the native slender swimmer. When the foil length is constant at L, the projected length L_s of the undulated foil on the streamwise direction is time dependent, $L_s(t) \leq L$ in one oscillation period. The time-mean value of $L_s(t)$ declines with decreasing λ.

We home in on the effect of St, Re and λ on thrust generation, added mass, added damping, efficiency and wake structures of the foil. The time-mean thrust $\bar{C}_T$ is mapped on the St–Re plane for different λ values. A unifying mechanistic relationship of $\bar{C}_T$ with St, Re and λ is obtained as $\bar{C}_T = 0.36Re^{0.208}St^3\lambda - 6.13Re^{-0.6}$. The value of $\bar{C}_T$ increases with increasing St, Re and λ. The enhancement of $\bar{C}_T$ with Re rapidly degrades for $Re \leq 250{-}600$ (depending on St), being negligibly small for $Re \geq 250{-}600$. On the other hand, the enhancement of $\bar{C}_T$ with St is higher at a higher Re and larger λ. That is, a prey, being smaller, gets the benefits of $\bar{C}_T$ enhancement at smaller Re while a predator gets advantages of a higher $\bar{C}_T$ enhancement with St at a higher Re. A predator–prey game at a sufficiently high Re relies on St and λ only as the Re effect on $\bar{C}_T$ is negligible at a high Re. The unifying relationship also provides the scaling law of the drag–thrust boundary ($\bar{C}_T = 0$) that is marked as $St = 2.57Re^{-0.27}\lambda^{-1/3}$. An increase in λ advances the drag–thrust boundary to smaller Re and St values. The decreasing λ leads to a smaller fluctuation in thrust. A swimmer may have a more steady thrust when λ is smaller, consistent with the swimming behaviour of the *anguilliform* swimmer. On the contrary, a larger λ enhances the maximum instantaneous thrust, which explains why a slender swimmer adopts the C-start strategy during the survival behaviour. The foil with $\lambda > 100$ behaves similarly to that with $\lambda = \infty$. The analysis of the local time-mean pressure thrust along the foil suggests that the posterior body of the foil dominates the pressure thrust generation at $\lambda = 0.50$, while the mid and posterior bodies show similar contributions to pressure thrust at $\lambda = 2.0$. The local time-mean friction thrust is negative over the entire length of the foil, and its magnitudes near the leading and trailing edges of the foil decrease and increase, respectively, with increasing λ. The added mass ratio enhances with increasing St and λ but declines with increasing Re. At a sufficiently large Re (> 500), the viscous effect on added mass is negligible while λ has a strong effect on m_a^*. A longer λ yields a larger m_a^*. As such, a longer tail or a longer swimming body adopts small λ. The travel of the foil wave in the streamwise direction is predominantly attributed to the thrust generation for a short λ while both streamwise and lateral motion of the foil contribute to the thrust generation for a long λ. The added damping, largely negative, linearly decreases with increasing St or Re, while the decrease rate is larger at a larger λ. The contribution by the flow is constructive to $\bar{C}_T$ when St, Re and λ all are increased. This work provides a physical basis for understanding the swimming behaviour of aquatic animals.

Seven distinct wake structures are identified, namely steady, q-KV, q-RKV, KV, 2S, RKV and s-RKV wakes. Among them, the steady, q-KV, KV and 2S wakes are always drag producing while the q-RKV and RKV wakes can produce both drag and thrust depending on λ. On the other hand, the s-RKV wake is always thrust producing. When λ is smaller, the s-RKV wake transmutes into RKV, hence the s-RKV wake disappears at the $\lambda = 0.50$ examined. A smaller λ enhances the stability of the wake to not be slanted, deferring the RKV–s-RKV wake boundary, KV–RKV wake boundary and drag–thrust boundary.

Funding. The authors wish to acknowledge the support given by Research Grant Council of Shenzhen Government through grant JCYJ20180306171921088, by the National Natural Science Foundation of China through Grants 11672096 and 91752112 and by the Khalifa University of Science and Technology through Grants CIRA-2020-057.

Declaration of interest. The authors report no conflict of interest.

Author ORCIDs.
Li-Ming Chao https://orcid.org/0000-0002-8800-6065;
Md. Mahbub Alam https://orcid.org/0000-0001-7937-8556.

Appendix A

A.1. Effects of swimming amplitude and wavelength on thrust, efficiency and wake structure

Floryan, Van Buren & Smits (2019) reported that the foil efficiency can be increased by increasing the trailing edge amplitude of a flapping foil at a given St. This may not be the case for a travelling wavy foil. To understand how a_1 affects the thrust and efficiency for the travelling wavy foil, we investigated thrust and efficiency for $a_1 = 0.05$, 0.10, 0.15 and 0.20, and $\lambda = 0.50$, 0.67, 1.0, 1.5 and 2.0 at $St = 0.5$, $Re = 1000$.

With increasing a_1 or decreasing λ, the projected length (L_s) of the foil in the streamwise (x) direction shortens because of more foil length getting involved in the vertical (y) direction (2.1). Figure 22 demonstrates the effects of a_1 and λ on $\bar{C}_T$ and η of the travelling wavy foil at (St, Re) = (0.5, 1000). The value of $\bar{C}_T$ increases with λ but linearly decreases with a_1 (figure 22a,c). This observation suggests that a sufficiently smaller a_1 and a sufficiently larger λ are required to produce thrust. For example, the travelling wavy foil with the smallest $\lambda = 0.50$ examined cannot generate thrust ($\bar{C}_T > 0$) at the smallest $a_1 = 0.05$ examined. A further reduction in a_1 (< 0.05) at $\lambda = 0.50$ is required to generate thrust. With increasing λ, the drag–thrust boundary ($\bar{C}_T = 0$) moves to a larger a_1, such as $a_1 = 0.07$ for $\lambda = 0.67$ and $a_1 = 0.138$ for $\lambda = 1.0$. For a constant St (2.2), an increase in the amplitude must be accompanied by a decrease in the frequency. Figure 22(a,c) indicates that an increase in amplitude reduces thrust. One can therefore understand from (2.2) that the frequency must be increased to compensate for the decreased thrust, given a constant St.

The dependence of η on a_1 is shown in figure 22(b,d), where η monotonically decreases with increasing a_1 at $\lambda = 0.05$, 0.67 and 1.0 but first increases and then decreases for $\lambda = 1.5$ and 2.0. The peak efficiency is attained at $a_1 = 0.10$ and 0.15 for $\lambda = 1.5$ and 2.0, respectively. This phenomenon can be understood from the characteristics of the travelling wavy motion. On the one hand, the foil requires more power to generate a complicated travelling wavy motion at a smaller λ and/or a larger a_1. On the other hand, increasing a_1 hinders the flow passing around the foil. At a larger λ, an improvement in η can, therefore, be achieved through increasing a_1 before it declines with further increasing a_1 while at a smaller λ, η monotonically declines with a_1. The shift in the η peak to a higher a_1 value with increasing λ further proves that η at $\lambda \to \infty$ (purely pitching) would monotonically keep increasing with increasing a_1 (Floryan *et al.* 2019). Observations of swimming behaviours of aquatic animals further revealed that a larger a_1 may not necessarily produce a higher η (Rohr & Fish 2004). A large tail-beating amplitude is usually employed during the predator–prey behaviour, such as the C-start (Gazzola *et al.* 2012).

The dependence of wake structure on a_1 at different λ values is presented in figure 23. When a_1 is increased from 0.05 to 0.20 at $\lambda = 0.50$ and 0.67 (figure 23$a1$–$d1$, $a2$–$d2$), (i) the wake modifies from RKV to KV, (ii) the lateral width of the two vortex rows expands and (iii) the spatial wavelength of the vortex streets grows, i.e. the number of vortices declines. All these modifications explain the rapid decrease in η and $\bar{C}_T$ with increasing

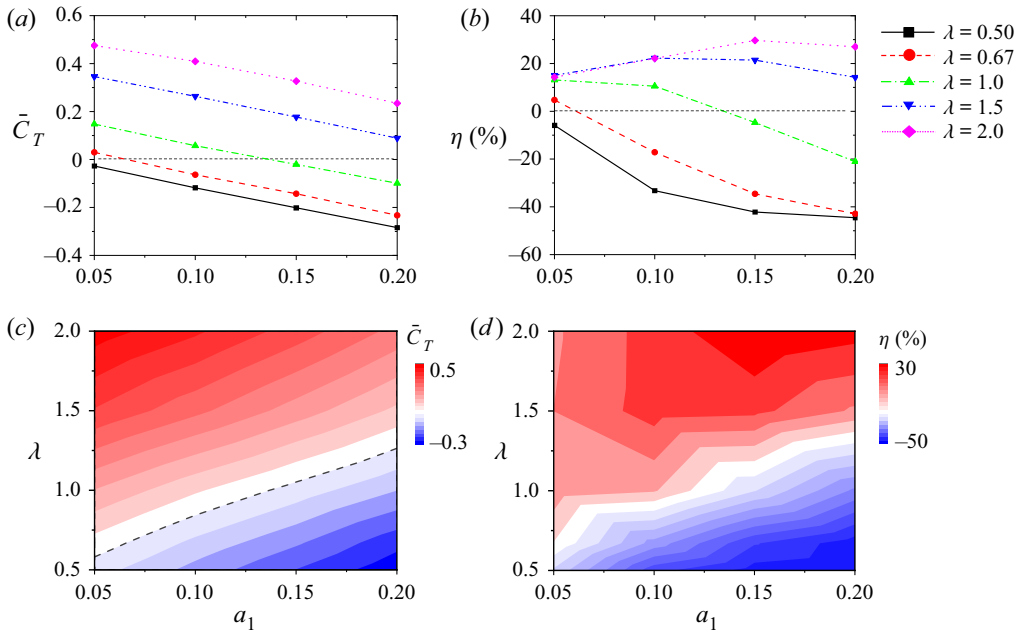

Figure 22. Dependence of (*a*) $\bar{C}_T$ and (*b*) η on a_1, and contours of (*c*) $\bar{C}_T$ and (*d*) η in the a_1–λ plane, where the black dashed line in (*c*) denotes the drag–thrust boundary; (St, Re) = (0.5, 1000).

a_1 (figure 22). The expansion of the lateral width with increasing a_1 is easily understood while the declination of the number of vortices is attributed to the decreased oscillation frequency, given a constant St. At $\lambda = 1.0$, the inversion of vortex streets does not happen, i.e. RKV wake remains RKV (figure 23*a*3–*d*3). The lateral distance between the two vortex streets, however, extends with a_1. On the other hand, at $\lambda = 1.5$ and 2.0, the increase in a_1 causes transmutation of the s-RKV wake into the RKV wake (figure 23*a*4–*d*4, *a*5–*d*5).

A.2. Validation for laminar flow assumption

In Xiao *et al.*'s (2011) work, the authors did not compare the numerical results between the laminar flow model and turbulence model. They assumed laminar flow based on the biological investigation of Anderson, McGillis & Grosenbaugh (2001) and the numerical study of Flanagan (2004). Anderson *et al.* (2001) examined tangential and normal velocity profiles of the boundary layers generated around two different swimming fishes, including a *carangiform* swimmer scup *Stenotomus chrysops* and an *anguilliform* swimmer smooth dogfish *Mustelus canis*. The boundary layer profile shape corresponded to laminar flow when the swimmer cruises in still water. In the present work, the NACA0012 foil undulating in the oncoming uniform flow is essentially similar to a fish swimming in still water. Moreover, Flanagan's (2004) work also suggested that the laminar boundary layer is valid up to a Reynolds number of 45 000.

To validate the laminar flow assumption, we have simulated thrust generation with two different turbulence models, including SA (Spalart & Allmaras, 1992) and k–ω SST (Wilcox, 1998) models, at (St, Re, λ) = (0.23, 45 000, 1.15) and (St, Re, λ) = (0.5, 2000, 1.0) and compared the results with those from the laminar flow model in table 3. The differences in the $\bar{C}_T$ results between the SA, k–ω SST and laminar models are less than 1 %. It suggests that the laminar flow assumption is valid at both Re values.

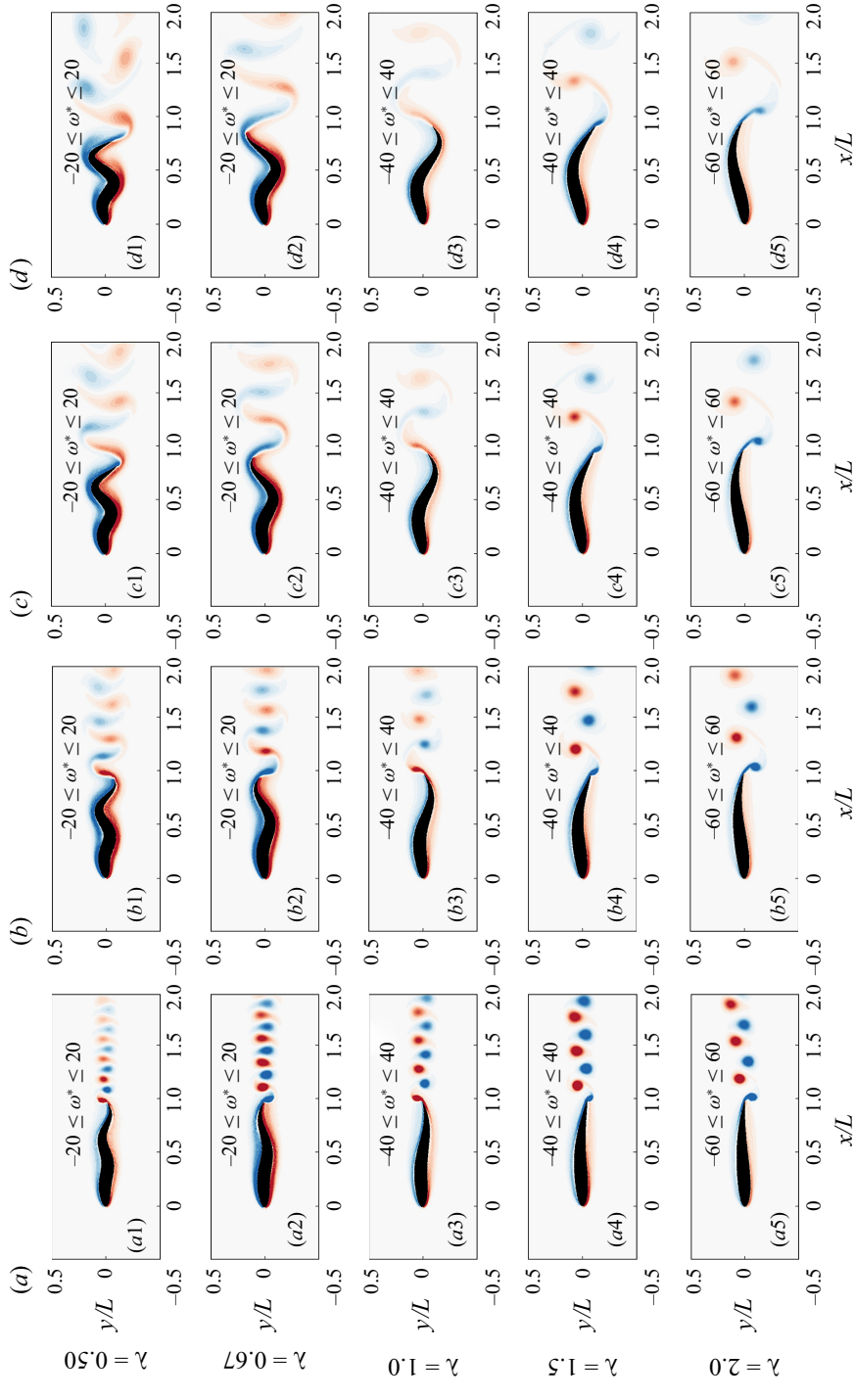

Figure 23. Effect of a_1 on the flow patterns; $(St, Re) = (0.5, 1000)$ with (*a*) $a_1 = 0.05$, (*b*) $a_1 = 0.10$, (*c*) $a_1 = 0.15$ and (*d*) $a_1 = 0.20$.

	Numerical model	$\bar{C}_T$	Difference in $\bar{C}_T$ (%)
$(St, Re, \lambda) = (0.23, 45\,000, 1.15)$	SA turbulence	0.04058	0.9532
	k–ω SST turbulence	0.03988	0.7927
	Laminar	0.0402	–
$(St, Re, \lambda) = (0.5, 2000, 1.0)$	SA turbulence	0.14836	0.6069
	k–ω SST turbulence	0.14694	0.3544
	Laminar	0.14784	–

Table 3. Different numerical models for the thrust generation.

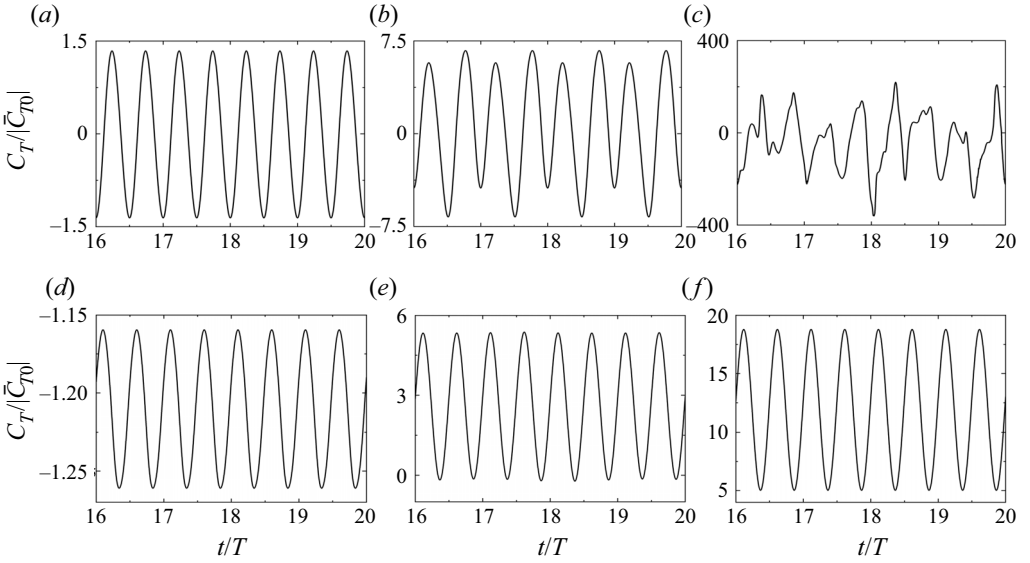

Figure 24. (*a–c*) Three types of thrust signals derived from a pitching foil at $Re = 1173$ (Godoy-Diana, Aider & Wesfreid 2008), for (*a*) periodic signal at $St = 0.2848$, (*b*) quasi-periodic signal at $St = 0.561$ and (*c*) non-periodic signal at $St = 1.615$. (*d*,*e*) Periodic signals from current travelling wavy foil at $Re = 1000$ and $\lambda = 1.0$ with (*d*) $St = 0.1$, (*e*) $St = 0.5$ and (*f*) $St = 1.0$. Here, $\bar{C}_{T0}$ is the drag force acting on a stationary foil.

A.3. Discussion on the instantaneous thrust coefficient

Pitching or undulating motion generally produces two thrust waves in one oscillation period, one in the upstroke and the other in the downstroke. Based on the difference in thrust peaks between the two waves, Godoy-Diana *et al.* (2008), for a pitching foil, observed three different types of thrust signals: periodic, quasi-periodic and non-periodic (figure 24*a–c*). We observed periodic thrust signals for the travelling wavy foil with $0.1 \leq St \leq 1.0$ (figure 24*d–e*), similar to the case of a pitching foil with smaller St (Figure 24*a*). The quasi-periodic thrust signal, occurring for moderate St, refers to the case where two thrust peaks are not the same (Figure 24*b*). For a large St, the thrust signal becomes non-periodic because of strong wake interactions (Figure 24*c*). Overall, the thrust signal would be transformed as the periodic → quasi-periodic → non-periodic signals when the wake interaction intensifies. Figure 24(*d–f*) shows the thrust signals derived from the present travelling wavy foil at $Re = 1000$ and $\lambda = 1.0$, where the thrust signals are periodic at the three examined $St = 0.1$, 0.5 and 1.0. This result suggests that a fish can

actively control the flow around itself using travelling wavy motion (Fish & Lauder 2006) to generate a more steady thrust compared with the case of pitching motion.

References

Alam, M.M. 2022 A note on flow-induced force measurement of oscillating cylinder by loadcell. *Ocean Engng* **245**, 110538.

Alam, M.M. & Muhammad, Z. 2020 Dynamics of flow around a pitching hydrofoil. *J. Fluids Struct.* **99**, 103151.

Andersen, A., Bohr, T., Schnipper, T. & Walther, J.H. 2017 Wake structure and thrust generation of a flapping foil in two-dimensional flow. *J. Fluid Mech.* **812**, R4.

Anderson, E.J., Mcgillis, W.R. & Grosenbaugh, M.A. 2001 The boundary layer of swimming fish. *J. Exp. Biol.* **204**, 81–102.

Barrett, D.S., Triantafyllou, M.S., Yue, D.K.P., Grosenbaugh, M.A. & Wolfgang, M.J. 1999 Drag reduction in fish-like locomotion. *J. Fluid Mech.* **392**, 183–212.

Bhatt, R. & Alam, M.M. 2018 Vibration of a square cylinder submerged in a wake. *J. Fluid Mech.* **853**, 301–332.

Bos, F.M., Lentink, D., van Oudheusden, B. & Bijl, H. 2008 Influence of wing kinematics on aerodynamic performance in hovering insect flight. *J. Fluid Mech.* **594**, 341–368.

Breder, C.M. 1926 The locomotion of fish. *Zoologica* **4**, 159–256.

Candelier, F., Boyer, F. & Leroyer, A. 2011 Three-dimensional extension of Lighthill's large-amplitude elongated-body theory of fish locomotion. *J. Fluid Mech.* **674**, 196–226.

Carling, J., Williams, T.L. & Bowtell, G. 1998 Self-propelled anguilliform swimming: simultaneous solution of the two-dimensional Navier-Stokes equations and Newton's laws of motion. *J. Expl Biol.* **201**, 3143–3166.

Chao, L.-M., Alam, M.M. & Ji, C. 2021*a* Drag-thrust transition and wake structures of a pitching foil undergoing asymmetric oscillation. *J. Fluids Struct.* **103**, 103289.

Chao, L.-M., Alam, M.M., Ji, C. & Wang, H. 2021*b* Flow map of foil undergoing fast and slow pitching. *Phy. Fluids* **33**, 101902.

Chao, L.-M., Cao, Y.-H. & Pan, G. 2017 A review of underwater bio-mimetic propulsion: cruise and fast-start. *Fluid Dyn. Res.* **49**, 044501.

Chao, L.-M., Pan, G., Zhang, D. & Yan, G.-X. 2019 Numerical investigations on the force generation and wake structures of a nonsinusoidal pitching foil. *J. Fluids Struct.* **85**, 27–39.

Dabiri, J.O. 2009 Optimal vortex formation as a unifying principle in biological propulsion. *Annu. Rev. Fluid Mech.* **41**, 17–33.

Das, A., Shukla, R.K. & Govardhan, R.N. 2016 Existence of a sharp transition in the peak propulsive efficiency of a low-*Re* pitching foil. *J. Fluid Mech.* **800**, 307–326.

Deng, J., Shao, X.M. & Ren, A.L. 2006 Numerical Study on propulsive performance of fish-like swimming foils. *J. Hydrodyn.* **18**, 681–687.

Deng, J., Sun, L.P. & Shao, X.M. 2015 Dynamical features of the wake behind a pitching foil. *Phys. Rev* E **92**, 063013.

Deng, J., Sun, L.P., Teng, L.B., Pan, D.Y. & Shao, X.M. 2016 The correction between wake transition and propulsive efficiency of a flapping foil: a numerical study. *Phys. Fluids* **28**, 094101.

Dong, G.J. & Lu, X.Y. 2005 Numerical analysis on the propulsive performance and vortex shedding of fish-like travelling wavy plate. *Intl J. Numer. Methods Fluids* **48**, 1351–1373.

Eloy, C. 2012 Optimal Strouhal number for swimming animals. *J. Fluids Struct.* **30**, 191–202.

Facchinetti, M.L., de Langre, E. & Biolley, F. 2004 Coupling of structure and wake oscillators in vortex-induced vibrations. *J. Fluids Struct.* **19**, 123–140.

Fish, F.E. & Lauder, G.V. 2006 Passive and active flow control by swimming fishes and mammals. *Annu. Rev. Fluid Mech.* **38**, 193–224.

Flanagan, P.J. 2004 Unsteady Navier–stokes simulation of rainbow trout swimming hydrodynamics. MSc thesis, Washington State University, Department of Civil and Environmental Engineering.

Floryan, D., van Buren, T., Rowley, C.W. & Smits, A.J. 2017 Scaling the propulsive performance of heaving and pitching foil. *J. Fluid Mech.* **822**, 386–397.

Floryan, D., van Buren, T. & Smits, A.J. 2019 Large-amplitude oscillations of foils for efficient propulsion. *Phys. Rev. Fluids* **4**, 093102.

Floryan, D., van Buren, T. & Smits, A.J. 2020 Swimmer's wake structures are not reliable indicators of swimming performance. *Bioinspir. Biomim.* **15**, 024001.

GAZZOLA, M., ARGENTINA, M. & MAHADEVAN, L. 2014 Scaling macroscopic aquatic locomotion. *Nat. Phys.* **10**, 758–761.

GAZZOLA, M., VAN REES, M. & KOUMOUTSAKOS, P. 2012 C-start: optimal start of larval fish. *J. Fluid Mech.* **698**, 5–18.

GODOY-DIANA, R., AIDER, J.-L. & WESFREID, J.E. 2008 Transitions in the wake of a flapping foil. *Phys. Rev.* E **77**, 016308.

GODOY-DIANA, R., MARAIS, C., AIDER, J.-L. & WESFREID, J.E. 2009 A model for the symmetry breaking of the reverse Bénard-Von Kármán vortex street produced by a flapping foil. *J. Fluid Mech.* **622**, 23–32.

GRAY, J. 1933 Studies in animal locomotion: I, the movement of fish with special reference to the eel. *J. Expl Biol.* **10**, 88–104.

GUPTA, S., SHARMA, A., AGRAWAL, A., THOMPSON, M.C. & HOURIGAN, K. 2021 Hydrodynamics of a fish-like body undulation mechanism: scaling laws and regimes for vortex wake modes. *Phys. Fluids* **33**, 101904.

HAN, P. & DE LANGRE, E. 2022 There is no critical mass ratio for galloping of a square cylinder under flow. *J. Fluid Mech.* **931**, A45.

KERN, S. & KOUMOUTSAKOS, P. 2006 Simulations of optimized anguilliform swimming. *J. Expl Biol.* **209**, 4841–4857.

KINSEY, T. & DUMAS, G. 2008 Parametric study of an oscillating airfoil in a power-extraction regime. *AIAA J.* **46**, 1318–1330.

KONSTANTINIDIS, E., DOROGI, D. & BARANYI, L. 2021 Resonance in flow-induced in-line vibrations at low Reynolds number. *J. Fluid Mech.* **907**, A34.

KOOCHESFAHANI, M.M. 1989 Vortical patterns in the wake of an oscillating airfoil. *AIAA J.* **27**, 1200–1205.

LAUDER, G.V. 2009 Swimming hydrodynamics: ten questions and the technical approaches needed to resolve them. *Exp Fluids* **51**, 23–35.

LAUDER, G.V. 2015 Fish locomotion: advances and new directions. *Annu. Rev. Mar. Sci.* **7**, 521–545.

LIAO, J.C., BEAL, D.N., LAUDER, G.V. & TRIANTAFYLLOU, M.S. 2003 Fish exploiting vortices decrease muscle activity. *Science* **302**, 1566–1569.

LIGHTHILL, M.J. 1969 Hydromechanics of aquatic animal propulsion. *Annu. Rev. Fluid Mech.* **1**, 413–446.

LIGHTHILL, M.J. 1970 Aquatic animal propulsion of high hydromechanical efficiency. *J. Fluid Mech.* **44**, 265–301.

LINDSEY, C.C. 1978 Form, function and locomotory habits in fish. In *Fish Physiology Locomotion*, (ed. W. Hoar & D. Randall). Academic Press.

LU, X.Y. & YIN, X.Z. 2005 Propulsive performance of a fish-like travelling. *Acta Mech.* **175**, 197–215.

LUCAS, K.N., JOHNSON, N., BEAULIEU, W.T., CATHCART, E., TIRRELL, G., COLIN, S.P., GEMMELL, B.J., DABIRI, J.O. & COSTELLO, J.H. 2014 Bending rules for animal propulsion. *Nat. Commun.* **5**, 3293.

LUCAS, K.N., LAUDER, G.V. & TYTELL, E.D. 2020 Airfoil-like mechanics generate thrust on the anterior body of swimming fish. *Proc. Natl Acad. Sci. USA* **117** (19), 10585–10592.

MARAIS, C., THIRIA, J.E., WESFREID, J.E. & GODOY-DIANA, R. 2012 Stabilizing effect of flexibility in the wake of a flapping foil. *J. Fluid Mech.* **710**, 659–669.

MUHAMMAD, Z., ALAM, M.M. & NOACK, B.R. 2022 Efficient thrust enhancement by modified pitching motion. *J. Fluid Mech.* **933**, A13.

PANICCIA, D., GRAZIANI, G., LUGNI, C. & PIVA, R. 2021 On the role of added mass and vorticity release for self-propelled aquatic locomotion. *J. Fluid Mech.* **918**, A45.

PIÑEIRUA, M., GODOY-DIANA, R. & THIRIA, B. 2015 Resistive thrust production can be as crucial as added mass mechanisms for inertial undulatory swimmers. *Phys. Rev.* E **92**, 021001(R).

QIN, B., ALAM, M.M. & ZHOU, Y. 2017 Two tandem cylinders of different diameters in cross-flow: flow-induced vibration. *J. Fluid Mech.* **829**, 621–658.

ROHR, J.J. & FISH, F.E. 2004 Strouhal numbers and optimization of swimming by odontocete cetaceans. *J. Expl Biol.* **207**, 1633–1642.

SAPÈDE, D., GOMPEL, N., DAMBLY-CHAUDIÈRE, C. & GHYSEN, A. 2002 Cell migration in the postembryonic development of the fish lateral line. *Development* **129** (3), 605–615.

SHELLEY, M.J. & ZHANG, J. 2011 Flapping and bending bodies interacting with fluid flows. *Annu. Rev. Fluid Mech.* **43**, 449–465.

SHEN, L., ZHANG, X., YUE, D.K.P. & TRIANTAFYLLOU, M.S. 2003 Turbulent flow over a flexible wall undergoing a streamwise travelling wave motion. *J. Fluid Mech.* **484**, 197–221.

SHI, X.Y., ALAM, M.M. & BAI, H.L. 2020*a* Wakes of elliptical cylinders at low Reynolds number. *Wind. Struct.* **30**, 525–532.

SHI, X.Y., ALAM, M.M., BAI, H.L. & WANG, H.F. 2020*b* The effect of Reynolds number on the elliptical cylinder wake. *Intl J. Heat Fluid Flow* **82**, 108553.

SHU, D.-G., LUO, H.-L., MORRIS, S.C., ZHANG, X.L., HU, S.-X., CHEN, L., HAN, J., ZHU, M., LI, Y. & CHEN, L.Z. 1999 Lower Cambrian vertebrates from South China. *Nature* **402**, 42–46.

SMITS, A.J. 2019 Undulatory and oscillating swimming. *J. Fluid Mech.* **874**, P1.

SPALART, P. & ALLMARAS, S. 1992 A one-equation turbulence model for aerodynamic flows. *AIAA Paper* 92-0439.

TAYLOR, G.K., NUDDS, R.L. & THOMAS, A. 2003 Flying and swimming animals cruise at a Strouhal number tuned for high power efficiency. *Nature* **425**, 707–711.

TRIANTAFYLLOU, M.S., TRIANTAFYLLOU, G.S. & YUE, D.K.P. 2000 Hydrodynamic of fishlike swimming. *Annu. Rev. Fluid Mech.* **32**, 33–53.

TRIANTAFYLLOU, M.S., WEYMOUTH, G.D. & MIAO, J.M. 2015 Biomimetic survival hydrodynamics and flow sensing. *Annu. Rev. Fluid Mech.* **48**, 1–24.

VAN BUREN, T., FLORYAN, D., QUINN, D. & SMITS, A.J. 2017 Nonsinusoidal gaits for unsteady propulsion. *Phys. Rev. Fluids* **2**, 053101.

VERMA, S., PAPADIMITRIOU, C., LÜTHEN, N., ARAMPATZIS, G. & KOUMOUTSAKOS, P. 2020 Optimal sensor placement for artificial swimmers. *J. Fluid Mech.* **884**, A24.

VIDELER, J.J. 1993 *Fish Swimming*. Chapman & Hall.

VON KÁRMÁN, T. & BURGERS, J.M. 1934 General aerodynamic theory-perfect fluids. In *Aerodynamic Theory* (ed. Durand). Stanford University.

WEBB, P.W. 1984 Forms and functions in fish swimming. *Sci. Am.* **251**, 72–82.

WILCOX, D.C. 1998 *Turbulence Modeling for CFD*. DCW Industries, Inc, LaCanada.

WILLIAMSON, C.H.K. & GOVARDHAN, R. 2004 Vortex-induced vibrations. *Annu. Rev. Fluid Mech.* **36**, 413–455.

WU, T.Y. 2011 Fish swimming and bird/insect flight. *Annu. Rev. Fluid Mech.* **43**, 25–58.

XIAO, Q., SUN, K., LIU, H. & HU, J. 2011 Computational study on near wake interaction between undulation body and a D-section cylinder. *Ocean Engng* **38**, 673–683.

ZHANG, J. 2017 Footprints of a flapping wing. *J. Fluid Mech.* **818**, 1–4.

ZHANG, D., PAN, G., CHAO, L.-M. & ZHANG, Y. 2018 Effects of Reynolds number and thickness on an undulatory self-propelled foil. *Phys. Fluids* **30**, 071902.

ZHENG, Z.C. & WEI, Z. 2012 Study of mechanisms and factors that influence the formation of vortical wake of a heaving airfoil. *Phys. Fluids* **24**, 103601.